UNIVERSITÀ DEGLI STUDI DI PADOVA

Dipartimento di Fisica e Astronomia 'Galileo Galilei'

Master Degree in Astrophysics and Cosmology

Final Dissertation

Analysis of Novae X-ray spectra in outburst and quiescence

Thesis supervisor   **Candidate**

Prof. Stefano Ciroi   **Canton Valentina**

Thesis co-supervisor

Dr. Marina Orio

Contents

Abstract

This thesis focuses on the study of two nova systems, one in a late phase of the outburst and the other returning to quiescence a few years after the outburst. I conducted X-ray spectral analyses of two systems: Nova V407 Lup and Nova YZ Ret 2020. V407 Lup is classified as an Intermediate Polar, while YZ Ret is identified as a VY Scl nova-like variable. The thesis is structured into four chapters.

The first chapter examines the main properties of Cataclysmic Variables, progenitors of the nova systems, and their spectral features in the X-ray and optical bands. The second one provides a detailed overview of the two X-ray observatories used to investigate Nova V407 Lup and YZ Ret: Chandra and XMM-Newton.

The third chapter focuses on V407 Lup and its spectral analysis. The goal was to confirm the magnetic nature of the white dwarf, supported by both timing and spectral analysis. The fitting of the XMM-Newton X-ray spectra suggests the possibility that the system contains a pulsar-like white dwarf.

The final chapter explores Nova YZ Ret, the first VY Scl type variable observed during a nova outburst. I analyzed the RGS XMM-Newton and Chandra LETG spectra, which revealed narrow Radiative Recombination Continua of CV, CVI, and NVI. This feature indicates a cold plasma component with $kT \sim 2\,\mathrm{eV}$ mixed with the collisionally ionized hot plasma at $kT \sim 70\,\mathrm{eV}$. In conclusion, this thesis presents detailed spectral of two unique novae, enhancing our understanding of their physical properties and evolutionary states. I am a co-author of two refereed articles regarding these targets, contributing to the field of CV research.

Chapter 1

Introduction

This chapter explores the fundamental characteristics of Novae, which can manifest as both symbiotic systems and Cataclysmic Variables (CVs). Symbiotic systems typically have longer orbital periods due to the presence of an evolved donor star, while CVs generally exhibit shorter periods, typically of the order of hours, as their secondary stars are typically main sequence stars. The initial sections (Sec.1.1 and Sec.1.2) explain more in detail the properties of cataclysmic variables and the mechanisms underlying the formation of accretion discs. Sec.1.3 zooms into Classical Novae, Nova-like variables and magnetic cataclysmic variables exploring the distinguishing traits of the two novae examined in this thesis. Specifically, Nova V407 Lup falls under the magnetic cataclysmic variables category, while YZ Ret is classified as a Nova-like variable. Lastly Sec.1.4 describes the formation of nova spectra and why observation in the X-Ray and optical band are essential to comprehend the physics behind these objects.

1.1 Cataclysmic variables

Cataclysmic variables are close binary system consisting of a primary star, a white dwarf (WD), and a secondary one, usually a lower mass main sequence star. The two components are generally separated by less than a few solar radii so their interaction occurs mainly via Roche-Lobe overflow, leading to the formation of an accretion disk around the equatorial zone of the WD if the star is non-magnetic. Instead, if the primary is strongly magnetized, the accreting material is forced to follow the fields lines falling on the magnetic poles of the WD [1]. If the WD magnetic field is strong enough, the interaction between the components of the binary system is

tidal, and force the secondary to rotate synchronously with the orbital revolution. The shapes of the orbits, also known as Roche equipotentials, are calculated imposing $\Phi_R = const$, where the Φ_R is the total potential at any point defined as the sum of the gravitational potential of the two stars and the effective potential of the fictitious centrifugal force. Φ_R is a function of the mass ratio q, defined as $\frac{M(2)}{M(1)}$, with M(1) and M(2) being the mass of the primary and the secondary respectively, and its scale is determined by a, the separation between the centers of mass of the binary components. Two main factors contribute in shaping the orbits: rotation, which flatten the star along its rotation axis, and tidal force, which stretches the star in the direction of its companion. As we can see from Fig.1.1 equipotential surfaces are almost spherical at the inner radius, while, if the secondary expands until it fills its Roche Lobe reaching the inner Lagrangian point L_1, they become more elongated. L_1 is the saddle point of Φ_R and lies in between the closed equipotential orbit of both stars where the effective attraction exactly balance. Material at L_1 is in equilibrium, but the slightest perturbation will move the mass from the Roche lobe of the secondary into the Roche lobe of the primary [2]. The deep potential well into which the accreting gas falls leads to high energy phenomena in the vicinity of the primary, with the result that CVs are luminous objects in the far ultraviolet and X-ray regions [3].

CVs are classified according to their different outburst phenomena. *Classical Novae (CN)* have only one observed eruption, but they are expected to recur. *Recurrent Novae (RN)* are similar to CN, but they undergo multiple nova eruptions over time, with a recurrence timescale of decades. *Dwarf Novae (DN)* exhibit semi-regular outbursts, with intervals ranging from 10 days to several years. Their brightness typically varies by 2-5 magnitudes during these outbursts. *Nova-like variables (NLS)* are non eruptive CVs with stable accretion disks, showing no significant outbursts. The last class are the *Magnetic CVs (mCVs)* in which the magnetic field of the primary can disrupt partially or totally the accretion disc [1, 4].

The period distribution of cataclysmic variables (CVs) exhibits several notable features. The maximum period observed in the majority of the systems is $\sim 12\,hr$. This can be explained by the relation between the mass of the secondary and the orbital period $M_2 \approx 0.1 P_{orb}$, where M_2 is in solar masses and P_{orb} is in hours. Given that the secondary star's mass is less than that of the white dwarf and also less than the Chandrasekhar mass $M_{Ch} \sim 1.44 M_\odot$, the mass-period
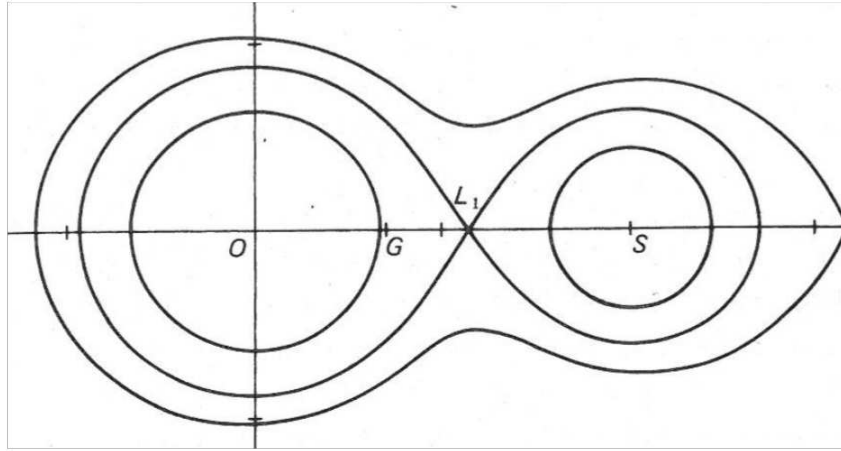
Figure 1.1: Roche lobe equipotentials. O and S are the centers of the primary and the secondary star respectively, while G is the center of gravity. The mass ratio q is 0.5 and L1 is the inner Lagrangian point. From [2].

relation provides maximum P_{orb} values of 12 hours [1]. Observations indicate also the presence of a period minimum at $P_{orb} \approx 80\,min$. This minimum period is associated with the secondary star departing from thermal equilibrium until its core becomes degenerate and dominated by the electron degeneracy pressure. At this point the typical mass-radius relation for a main sequence star is replaced with $R \propto M^{-1/3}$causing the star to expand in response to mass loss. Consequently, the binary orbit and period increase to accommodate the secondary star [1, 5].

One of the most intriguing features in the period distribution of CVs is the *period gap* between 2 and 3 hours. Notably, there is a significant deficiency of non magnetic CVs within this range [4]. This gap is attributed to the cessation of mass transfer due to the loss of angular momentum driven by magnetic braking (MB) [6]. When the donor star in the binary system becomes fully convective at around $P_{orb} \simeq 3\,hr$, MB abruptly ceases, reducing the mass loss rate. As a result, the secondary star contracts and loses contact with the Roche lobe. During this phase, the loss of orbital angular momentum is governed by gravitational radiation. When $P_{orb} \simeq 2\,hr$ the Roche lobe shrinks sufficiently to re establish contact with the secondary [1, 5]. Using the SDSS I-IV catalogue, Schreiber et al. derived a more precise range for the period gap in cataclysmic variables, identifying it to be between 147 and 191 minutes. Observations have shown that within

the period gap, magnetic systems are more prevalent compared to non magnetic ones [7]. In cataclysmic variables with a high WD magnetic moment, MB is less effective, resulting in a less significant contraction of the donor star. Consequently, magnetic CVs re establish contact with the Roche lobe more quickly than their non magnetic counterparts [8].

1.2 Accretion Discs

CVs are unique natural laboratories to observe accretion discs. The inflowing gas stream from the secondary to the primary star of the binary system has a momentum predominantly in the orbital plane. Particles, captured by the gravitational field of the WD, tend to settle into circular orbit with a Keplerian angular velocity:

$$\Omega_K(r) = \sqrt{\frac{GM}{r^3}} \tag{1.1}$$

where M is the mass of the primary and r the distance in the radial direction. A fluid rotates differentially, so there must be a radial drift of material due to the viscous shear between adjacent layers. The energy of the shearing motion is dissipated in the fluid as heat and then radiated away [4]. Viscosity controls the outward diffusion of angular momentum in the radial direction, spreading the gas into an accretion disc. The surface density evolution is governed by the viscous timescale:

$$t_{\nu_{vis}}(r) = \frac{r^2}{\nu_{vis}} \tag{1.2}$$

where ν_{vis} is the viscosity. The dissipative processes spread the disc out, allowing the inner parts to move in as a consequence of the conservation of angular momentum. If the rate at which mass is transferred to the disc changes on a timescale longer than $t_{\nu_{vis}}$, than the disc settles into a steady state and from the mass conservation equation provides the mass flux:

$$\dot{M} = 2\pi r \Sigma(-v_{rad}) \tag{1.3}$$

where Σ is the surface density and v_{rad} [9]. The nova-like variable stars RW Tri, UX UMa, SW Sex, LX Ser, V1315 Aql and V363 Aur have steady-state bright discs and the mass overflow is thought to be driven by loss of angular momentum through magnetic braking [10].

The nature of viscosity ν_{vis} is not easy to be determined. Shakura and Sunyaev introduced a dimensionless parameter α, usually $\alpha \leq 1$, to take into account all the uncertainties. Detailed

models of CV discs found a value of α between 0.1 and 1 [11]. The authors defined ν_{vis} as follows:

$$\nu_{vis} = \alpha c_s H \tag{1.4}$$

in which c_s is the speed of sound and Eq.1.4 may be thought as the viscosity of a turbulent eddy of size H and turnover speed αc_s [12].

The spectrum emitted by an elemental area of the accretion disc at each radius, is a blackbody with temperature $T_s(R)$:

$$B_\nu(T_s) \propto \frac{\nu^3}{e^{\frac{h\nu}{kT_s}} - 1} \tag{1.5}$$

where k is the Boltzmann constant, h the Planck constant and ν the frequency. The whole spectrum S_ν is the integration of Eq.1.5 between the radius of the star R_* and the radius of the outer disc R_{out}:

$$S_\nu \propto \int_{R_*}^{R_{out}} B_\nu 2\pi R dR \propto \nu^{\frac{1}{3}} \int_0^{x_{out}} \frac{x^{\frac{5}{3}} dx}{e^x - 1} \tag{1.6}$$

where $x = \frac{h\nu}{kT}$, $x_{out} = \frac{h\nu}{kT_{out}}$ and T_{out} is the temperature evaluated at the outer radius of the disc. The functional form of S_ν is shown in Fig.1.2. Three different regions can be defined:

- If $\nu \gg \frac{kT}{h}$ the spectrum drops exponentially and the emission comes from the hottest regions of the disc.

- If $\frac{kT_{out}}{h} \ll \nu \ll \frac{kT}{h}$, then $x_{out} \gg 1$ and $S_\nu \propto \nu^{1/3}$ [13].

- If $\nu \ll \frac{kT_{out}}{h}$, the Rayleigh-Jeans tail of the coolest elements of the disc dominates and $S_\nu \propto \nu^2$ [9].

Disc instabilities are responsible for the flickering phenomenon from CVs discs [14]. These instabilities are mainly due to convective and tidal effects [11].
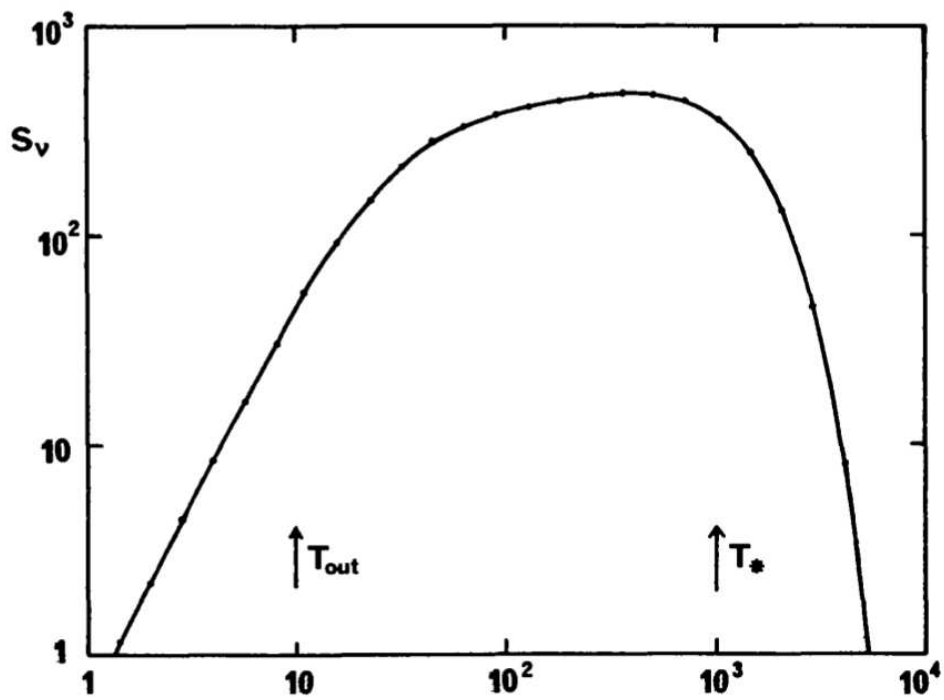
Figure 1.2: Integrated spectrum of a steady accretion disc that radiates a local blackbody spectrum at each point. The units are arbitrary, but the frequencies corresponding to T_{out}, te temperature of the outermost disc radius, and to T_*, the characteristic temperature of the inner disc, are marked [9].

1.3 Classification of CVs

1.3.1 Classical Novae

Gas lost by the secondary star is accreted onto the WD surface and gradually forms a layer of fuel. The bottom of this hydrogen-rich blanket is compressed by both strong gravity of the WD and constantly infalling material, leading the electrons in the ionized hydrogen to become degenerate [15]. As the layer thickens, the temperature at its base increases until it will become high enough to the beginning of hydrogen fusion. Since the pressure in a degenerate gas is independent of temperature, the onset of burning leads to a rise in temperature which is not balanced by thermal expansion causing a thermonuclear runaway (TNR) and a classical nova explosion (CNe) [1]. The temperature in the nuclear burning region is larger than 10^8 K if $M_{WD} \leq 1.0 M_\odot$, while can exceed $\sim 10^8$ K for higher mass WDs, $M_{WD} \geq 1.2 M_\odot$ [15]. The proton-proton chain ($p + e^- + p \rightarrow d + \nu$) generates energy only during the accretion phase of the outburst, before the rise of the TNR. When the temperature at the base of the envelope rises to $2 \cdot 10^7$ K, CNO cycle sets on and power the final stage and the evolution to the peak of the TNR [15, 4]. Mixing of the WD outer layers with the accreted matter ensures that a sufficient number of C, N and O nuclei can act as a catalyst during the CNO cycle [16]. The behavior of a CN event is determined by three main factors: the mass of the WD (M_{WD}) the temperature of the WD (T_{WD}) and the accretion rate from the companion ($\dot{M}$) [1, 17].

Instantly after a CN outburst the mass ejected is optically thick. When it becomes optically thin we are able to detect the WD as a super soft X-ray source (SSS). Later, the X-ray luminosity powered by the hydrogen-rich remnant decreases and the CN event ends. The mass ejected into the ISM during the outburst ranges between $\sim 10^{-7} M_\odot$ and $\sim 10^{-4} M_\odot$ [18]. This remnant envelope mass is expected to undergo stable hydrogen burning throughout the SSS phase at a nearly constant bolometric luminosity, until the WD atmosphere contracts to the pre-outburst radius. This phase can last from almost ten years for $M_{WD} \approx 0.60 M_\odot$ to several days for $M_{WD} \approx 1.30 M_\odot$ [19]. Continued accretion from the secondary on the WD surface provides a source of hydrogen-rich fuel, triggering a new CN outburst. The recurrence time expected between two nova eruptions is proportional to the critical mass of the envelope and the mass accretion rate of the WD [4].

Novae are typically classified into different speed classes based on t_2 and t_3, which are the times required to fade by 2 or 3 magnitudes respectively from the visual maximum. Slow novae have $t_2 \geq 80$ days, while for fast novae $t_2 \leq 80$ days [20]. In the past these times were used to obtain a rough estimation of novae distances through the maximum magnitude rate of decay (MMRD) relation [21]. Nowadays this correlation is no longer applied, due to its huge scatter, and nova distances are determined using the parallaxes calculated by the Gaia spacecraft [22].

CN outbursts can also occur in symbiotic systems, in which the secondary is an evolved giant star. Their period are usually longer than 100 days [23].

1.3.2   Magnetic CVs

Magnetic CVs are a class of cataclysmic variables distinguished by the presence of a magnetized WD. These systems constitute $\sim 20 - 25\%$ of all CVs [24] and they are further divided into two groups depending on the WD magnetic field intensity: *Intermediate Polars (IP)* and *Polars* [4].

Intermediate Polars are also known as DQ Her systems, they have orbital periods $P_\Omega \geq 4\,hr$ and their magnetic field strengths are in the range $\sim 5 - 20\,MG$ [24]. At these magnetic field intensities, the two components of the binary system do not become locked into synchronous rotation. Consequently, we observe two distinct periods: the spin period P_ω of the WD and the orbital period of the binary system. Typically is $P_\omega \ll P_\Omega$. Modulations in the X-ray flux can be detected both at the spin and the orbital periods. The modulation at P_ω derives from the misalignment between the magnetic and the spin axis of the WD [25]. Instead the modulation at P_Ω is due to the photoelectric absorption, since its depth decreases with the increase of the X-ray energy [26]. IPs show accretion discs truncated at the Alfven radius R_A, where the ram pressure of the infalling gas and the magnetic pressure of the WD are in equilibrium [4].

Polars, also known as AM Her-type variables, show the presence of polarization at optical and near-IR wavelengths. They dominate the period distribution at $P_\Omega \leq 4\,hr$ [24]. Their strong magnetic fields, $B \sim 10 - 230\,MG$ [27], are able to synchronize the two periods P_ω and P_Ω and also prevent the formation of an accretion disk. The infalling gas from the companion is channeled directly to the magnetic poles of the WD by the field lines [4].

As the accretion flow approaches the WD surface, it becomes highly supersonic and produces a strong shock in a region close to the star. The accreting matter turns into a dense, subsonic and hot plasma with $T \sim 10^8$ K, which radiates hard X-rays at the shock front [28]. The majority of the X-ray flux emerges from the $\sim 10\%$ of the WD surface [29]. The post-shock plasma cools down via thermal bremsstrahlung in IPs [30] and via cyclotron emission in polars, due to their high magnetic fields [31]. A fraction of these radiation is intercepted and thermalized by the WD surface producing an optically thick emission in the soft X-rays, which can be modeled as a blackbody with $T \sim 10^5$ K [32]. This component is a characteristic feature of polars spectra [27]. IPs instead emit mostly in the hard X-rays, however some of them show a soft X-ray component in the $30 - 100$ eV. These systems are classified as *soft-IPs* [33]. Another characteristic of the mCVs is the emission of the Fe $K\alpha$ lines, which results from hard X-rays generated in the accretion column being reflected off the white dwarf surface. The $K\alpha$ lines can be resolved into three distinct components: fluorescence at 6.4 keV, He-like at 6.7 keV and H-like at 7.0 keV lines [28].

The post shock region (PSR) is described by the mass continuity, the momentum and the energy equation and by the ideal gas law [34]. The maximum temperature T_s of the PSR is strictly connected to the WD mass and can be estimated using the Rankine-Hugoniot conditions for a strong shock:

$$kT_s = \frac{3GM_{WD}\mu m_H}{8R_{WD}} \qquad [keV] \tag{1.7}$$

[35], where M_{WD} and R_{WD} are the mass and radius of the WD, μ is the mean molecular weight and m_H is the mass of hydrogen atom. Using this relation we can easily determined the WD mass. Eq.1.7 holds in the case of a pre-shock gas having a free-fall velocity from infinity. Since in polars and IPs the gas stream falls from the Alfvèn radius, the derived mass changes according to:

$$M_{WD}(R_A) = M_{WD}(\infty)\left(1 - \frac{R_{WD}}{R_A}\right) \tag{1.8}$$

where $M_{WD}(\infty)$ is the mass calculated at infinity [34]. WD masses of IPs were determined using the X-ray spectral data from the Swift/BAT survey and the values range from $\sim 0.5\,M_\odot$ to $\sim 1\,M_\odot$ [36].

The density of the post shock region ρ_{shock} can be determined from the mass accretion rate $\dot{M}$ as

follows:

$$\dot{M} = \rho_{shock} v_{ff} A \qquad (1.9)$$

where v_{ff} is the free-fall velocity and A the area of the accretion column.

The magnetic field of the white dwarf can impact nova outbursts. Specifically, a strong magnetic field can inhibit convection, thereby reducing the degree of mixing and weakening the thermonuclear runaway (TNR) [37]. On the other hand, IPs can enter in a fast magnetic rotator regime in which the ejection of all the accreted envelope is more rapidly and occurs even when the TNR is produced by a low degree of electron degeneracy [38].

1.3.3 Nova-like variables

Nova-like variables are characterized by the absence of disc instability-type outbursts, implying that their accretion discs are permanently in an hot state. To prevent thermal-viscous instabilities and achieve this quasi steady regime, the mass transfer from the secondary star $\dot{M}$ must overcome a critical value $\dot{M}_{crit} \sim 10^{-9.5} M_\odot \, yr^{-1}$ [39]. However some departures exist from the canonical steady state theory of the accretion discs. Rutten et al., using the eclipse maps, showed that the systems V1315 Aql and SW Sex exhibit a radial temperature dependence in the inner disc region much flatter than the theoretical one $T \propto R^{-3/4}$ [10]. Another deviation from the predicted accretion disc picture was found in the infrared (IR) band, which is dominated by the disc emission. The IR excess can originate from the circumbinary dust or from the bremsstrahlung produced by the accretion disc wind outflows [40]. Light curves of high inclination NLs reveal round-bottomed eclipses, which can be variable from cycle to cycle both in depth and shape. Eclipse maps show generally symmetric discs brighter in the center with respect to the edge. Periods of Nova-like systems lie above the period gap, between 3 and 4 hours. NLs are also classified into different sub-types according to their spectroscopic properties such as *SW Sex stars* or photometric variations such as *VY Scl* [41].

SW Sex stars are defined as eclipsing nova-like stars with single peaked Balmer and HeI emission lines. They are also identified by a narrow central absorption component in HI and HeI line cores, at typically around a photometric phase of $\phi = 0.5$, at the superior conjunction of the secondary star [4]. SW Sex-type stars are faint in X-rays. This may be due to the intrinsic ab-

sorption or, since they are high inclination systems, to the absorption by the accretion disk [42]. Variable circular polarization was found by Rodriguez et al. in V795 Herculis [43] and LS Pegasi [44]. The values of the WD's magnetic field were $\approx 5 - 15\,MG$ for LS Pegasi and $\approx 2 - 7\,MG$ for V795 Herculis, both consistent with what is found in IPs that show circular polarization. The magnetic properties of SW Sex stars leads to a new accretion scenario where a disc gas stream interacts with the white dwarf's magnetosphere, resulting in a shock above the disc. Schmidto-breick suggested that the SW Sex subclass could represent an evolutionary stage of cataclysmic variables (CVs). Given that CVs experience a transition from longer to shorter orbital periods due to angular momentum loss, and considering that all nova-like stars (NLs) with periods between $2.8 - 4\,hr$ are of SW Sex type, we can infer that CVs with periods $P \geq 4\,hr$ must evolve into the SW Sex regime before entering the period gap [45].

VY Scl spectra present high states, dominated by the emission of the accretion disk, and low states, in which the main component is the emission of the central WD. The latter are defined as the declining of more than 1.5 magnitudes in less than 150 days [39]. These drops in magnitude can reach 7 magnitudes and can last for years, as in the case of TT Arietis [46]. The origin of the VY Scl low states is the abrupt decline of the mass transfer rate $\dot{M}$, which can be explain in two different ways. The first involves the shielding of the WD radiation by the accretion disk [47], while the second accounts for the presence of star spots near the L_1 point and drifting across it [48].The sudden drop of the accretion rate should in principle cause viscous instability and consequently outbursts, which are not observed. Radiation from WDs with $T \approx 40000\,K$ are able to keep the inner disc in a hot state, avoiding the development of disc instabilities during the low states [49]. VY Scl low states allow us to determine the WD effective temperature and the mass transfer rate, since we can observe the WD directly.

1.4   Nova Spectra

Multiwavelength observations of novae provide new insights to understand the energetics of nova explosions, the composition of the ejected material and the interaction between the ejecta and the surrounding medium. Throughout my thesis, my primary focus was on analyzing X-ray spectra, while my collaborators concentrated on studying the optical band. X-Ray spectra offer

a window to observe directly the hydrogen burning WD during the SSS phase, probing its temperature, effective gravity and chemical composition.

Optical spectra are categorized in different phases according to the development of the nova outburst, namely the *pre-maximum*, *principal*, *diffuse enhanced*, *orion* and *nebular* phases [4]. The nature of the spectral lines appearing in the spectrum is determined by the evolution of the effective temperature of the radiation together with the decreasing of the shell density. Immediately after the outburst the high densities of the gas restrict the emission lines only to permitted transition of lower ionization. As the density in the expanding shell decreases, forbidden nebular lines emerge, e.g. $[NII]\lambda6584$, $[OIII]\lambda5007$, $[FeVII]\lambda6087$ and $[NeIII]\lambda3869$. The sudden absorption feature that appear in the Balmer and He I lines and the simultaneous presence of $FeII$, $OI\,\lambda8446$ and $[FeX]\lambda6375$ lines indicate the existence of inhomogeneities in the novae envelopes [50]. Old novae spectra suggest that the effects of the WD irradiation are significant even centuries after outburst. Features supporting this theory are the narrowness of $H\alpha$, the fading of the nebular lines and the presence of high-excitation lines even in the oldest novae [51]. The classification of novae in two spectral classes, namely *Fe II* and *He/N* novae, was proposed by Williams to explain the presence of the Balmer lines followed by the low-ionization Fe II lines or high-excitation He I, He II, N II and N III lines. However this classification was revisited by Aydi et al., which proved that the spectra naturally evolve from one type to another as the ejecta conditions change [52]. Velocities of the ejecta are slower in the Fe II phase, $FWHM \leq 2500\,km\,s^{-1}$, compared to He/N one, $FWHM \geq 2500\,km\,s^{-1}$. The two phases differ also in the line profiles. Fe II phase shows more P Cygni line profile, while He/N exhibit broad, flat-topped emission lines [53]. The evolution proceeds, as seen in Fig.1.3, throughout three main phases: *early He/N* phase, during the rise to the optical peak, *Fe II* phase, at the optical peak and the early decline, and the *late He/N* one throughout the late decline. The duration of these three stages is linked to the speed class of novae, especially the Fe II phase lasts only few hours for very fast novae such as V407 Lup [52].

The formation of *X-Ray* spectra proceeds through different phases as the nova eruption progresses [54]. Hours before the optical rise a short, bright and soft X-ray ($\leq 0.1\,\mathrm{keV}$) flash is detected, the so-called *fireball* phase. This thermal emission follows directly the runaway fusion, when the photosphere is expanding before the ejection of the envelope. The spectra re-
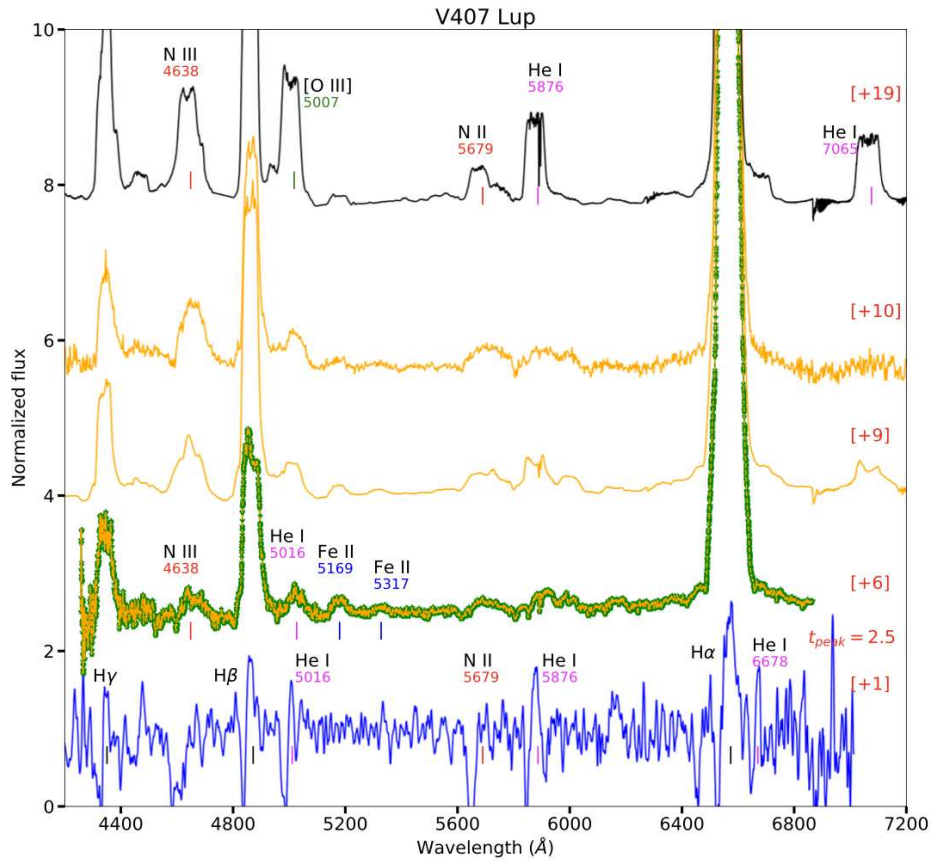
Figure 1.3: The overall spectroscopic evolution of nova V407 Lup representing the different spectral stages: phase 1 (early He/N), highlighted in blue; phase 2 (Fe II), highlighted in green; phase 3 (late He/N), highlighted in orange; and the nebular phase, highlighted in black. Numbers between brackets are days after t_0, the discovery date. Tick marks are presented under the lines for easier identification and they are color coded based on the line species. From [52].

sembles a blackbody with temperatures of $\sim 10^5\,\mathrm{K}$ and luminosities $L_X \sim 10^{38}\,erg\,s^{-1}$. The duration of the fireball phase is $\leq 8\,hr$ and it was only predicted by theoretical models since 2020, when it was detected in the nova YZ Reticuli [55, 56]. During the ejection of the envelope novae start to emit in hard X-rays ($\sim 1 - 10\,\mathrm{keV}$) and the spectrum enters in a *shock-dominated* phase. The radiation is consistent with a plasma in collisional ionization equilibrium and it is due to the strong shocks generated when the plasma outflowing the nova impact the circumbinary medium. This component is typically detected a month after the eruption and reaches luminosities $L_X \sim 10^{33-34}\,erg\,s^{-1}$ [57, 58, 59]. When the ejecta becomes optically thin appears the *super-soft (SSS)* phase ($\leq 0.5\,\mathrm{keV}$), which offers the opportunity to observe the nuclear burning

very close to the WD surface. Super-soft spectra exhibit a blackbody continuum with absorption or emission lines [60, 61].The last phase is the *accretion-powered* hard X-ray emission, typically $\geq 1\,\mathrm{keV}$. The radiation is produced by the boundary layer (BL), namely the inner region of the accretion disc when the gas stream from the secondary is shocked as it reaches the WD surface[62].

Chapter 2

X-Rays observatories and method of spectral analysis

In the opening paragraphs of this chapter, I present the two observatories used to investigate Nova V407 Lup and Nova YZ Ret, namely XMM-Newton and Chandra. Additionally, in Section 2.3, I explain the spectral analysis methodology. My collaborators employed the XMM SAS and CIAO software packages to extract the data, while I utilized `xspec` for analyzing X-ray spectra.

2.1   XMM-Newton X-Ray Observatory

XMM-Newton is an X-ray observatory launched by the European Space Agency (ESA) on December 10, 1999. It is named after Sir Isaac Newton and stands for *X-ray Multi-Mirror Mission*. The spacecraft, with its 4 tonne and 10 m long and it is the largest scientific satellite aver launched by ESA. XMM-Newton have six onboard instruments: three European Photon Imaging Camera (EPIC) CCDs, two Reflection Grating Spectrometer (RGS) units, and the Optical Monitor (OM), operating simultaneously and granting access to both X-ray and Optical/UV bands.

2.1.1   The X-ray telescopes

XMM-Newton is equipped with three X-ray telescopes, two of them carrying a *Reflection Grating Array (RGA)*. Each telescope, with a 7.5 m focal length, comprises a set of components, including baffles for both visible and X-ray suppression, a mirror module and an exit baffle ensuring optimal thermal conditions. Positioned before the mirror systems, X-ray baffles function

as collimators, minimizing stray light within the field of view (FOV) of the focal plane cameras.

Each mirror module is a grazing-incident Wolter I telescope, consisting of 58 gold-coated nested mirrors. Because of their high energy X-rays cannot be focused in the same way as visible light, so the optics must be aligned nearly parallel to the incoming light. Grazing incident mirrors are used to deflect X-rays at very shallow angles, allowing them to be focused onto detectors.The grazing angles ranging from 17' to 42', while the gold coating is crucial to provide a sufficient reflectivity at high energies and a very shallow reflection to X-ray at an angle of 30'. Each mirror shell is a paraboloid and an hyperboloid replicated together in one piece and it is 60 cm long. The outermost and innermost mirrors have a diameter of 70 cm and 30.6 cm respectively. They are most efficient in the energy range from 0.1 to 10 keV, with peak performance around 1.5 keV. The optics were designed to maximize the effective area across a broad energy spectrum, offering the largest collecting area of $1500\,cm^2$ for energies up to 150 eV and $350\,cm^2$ at 10 keV [63].

2.1.2   The European Photon Imaging Cameras (EPIC)

XMM-Newton's array of telescopes is outfitted with three *European Photon Imaging Cameras (EPIC)*: two of them are Metal Oxide Semi-conductor (MOS), while the third is a pn-CCD. These cameras facilitate high-sensitivity imaging observations across the telescope's expansive 30 arcmin FOV, covering a broad energy range from 0.15 to 15.0 keV. The spectral and angular resolutions are $\frac{E}{\delta E} \sim 20 - 50$ and $\sim 6'' FWHM$ respectively.

MOS CCD arrays are placed behind the telescopes and they are equipped with the gratings of the RGS, which direct the 44 % of the incoming flux towards the MOS cameras. There are seven EEV type 22 front-illuminated chip arrays in the focal plane of each camera and they are off-set with respect to each other in order to follow the focal surface curvature of the Wolter I telescopes. The MOS cameras detect photons at the softer portion of the X-ray spectrum, while they are less responsive for hard X-rays [64].

In contrast, the pn camera features a single silicon wafer integrating twelve 3 x 1 cm CCD chips. Unlike its MOS counterparts, the telescope housing the pn camera lacks gratings, ensuring that 100% of the X-rays are directed to the focal plane. The back-illuminated pn chip array is slightly

offset from the optical axis of its X-ray telescope to guarantee that $\geq 90\%$ of an on-axis point source is collected on a single pn CCD chip.

The EPIC cameras offer different data acquisition modes. For instance, the pn camera exclusively supports *full frame* and *extended full frame* modes, capturing all pixels of all CCDs across the entire FOV. Partial window mode, available for both MOS and pn cameras, enables versatile operation. In MOS cameras, the central CCD can operate in *small window mode* (100 x 100 pixels) or *large window mode* (300 x 300 pixels), whereas the pn camera's large window mode reads out half of the twelve CCDs' area. In *timing mode*, MOS and pn cameras operate simultaneously, facilitating one-dimensional imaging along the column axis.

2.1.3   The Reflection Grating Spectrometers (RGS)

The *Reflection Grating Spectrometers (RGS)* are positioned behind two of the three Wolter I type mirrors, where they disperse incoming light into multiple orders. They allow high resolution measurements, $\frac{E}{\delta E} \sim 100 - 500$, in the soft X-ray range from 5 to 35 Å or 2.5 to 0.33 keV and they are optimize to detect the transitions of C, N, O, N, Mg, Si and Fe. The RGS consist of two identical units and each unit includes an array of reflection gratings (RGA), which intercepts roughly half of the incoming beam and deflects it to the Focal Plane Camera (RFC). Undeflected light instead passes through where is detected by the EPIC-MOS in the telescope focal plane. Each RGA is made up of 182 identical diffraction grating plates each measuring 10 x 20 cm. The groove density is not constant across the grating surface and it is $\sim 645 \frac{lines}{mm}$ at the center. The gratings are mounted such that the incident and diffracted rays lie in a plane perpendicular to the grating grooves. The RFC contains a CCD bench formed by nine back-llluminated CCDs mounted in a row [65].

2.1.4   The Optical Monitor (OM)

The optical/UV Monitor (OM) Telescope covers UV and optical wavelengths from 170 to 650 nm and its FOV is 17'. Comprising a Telescope Module and a Digital Electronics Module, the OM features two identical units, facilitating simultaneous multiwavelength observations across X-ray and UV/optical bands.

The Telescope Module adopts a modified 30 cm Ritchey-Chretien design with a 3.8 m focal length.

Here, the incoming beam undergoes reflection first by the primary mirror, then directed onto the secondary mirror, and finally redirected by an inclined mirror towards the detector.

The Digital Electronics Module provides communications with the spacecraft and pre-process the data. [1]

2.2 Chandra X-ray Observatory

The Chandra X-ray Observatory, launched by the National Areonautics and Space Administration (NASA) on July 23, 1999, aims to capture X-ray radiation emanating from the universe's hottest regions. Positioned in a high elliptical Earth orbit reaching up to an altitude of 147,400 km, Chandra is equipped with a *High Resolution Mirror Assembly (HRMA)*, comprising a 10-meter focal length telescope. This assembly boasts four pairs of concentric thin-walled mirrors, crafted in a Wolter I type configuration, the largest of which boasts a diameter of 1.2 meters. Coated with iridium to enhance reflectivity in the X-ray spectrum, these mirrors are constructed from glass ceramic. Each mirror pair features a paraboloid at the front and a hyperboloid at the back, with inner and outer layers optimized for sensitivity to hard and soft X-rays, respectively. Achieving an impressive angular resolution of 0.5 arcseconds, HRMA offers an effective area of $800\,cm^2$ at 0.25 keV. It collaborates with four instruments, the ACIS and HRC imagers positioned in the focal plane, which capture mirror-formed images, and the LETG and HETG spectrometers, providing detailed insights into X-ray energy characteristics.

2.2.1 The Advanced CCD Imaging Spectrometer (ACIS)

The Advanced CCD Imaging Spectrometer (ACIS) is an array of ten CCDs, four front-illuminated chips disposed in a 2 x 2 array (ACIS-I) and six arranged in a 1 x 6 array (ACIS-S). ACIS-I produces optimal imaging, while ACIS-S is used for imaging or grating spectrum readout. The instrument provides position, energy and arrival time of individual incoming X-rays, allowing the simultaneous creation of images, spectroscopy and light curves. It is mostly used to examine temperature variations across the sources. ACIS-S can be used together with the *High Energy Transmission Grating (HETG)* to improve the resolving power up to 1000 in the energy range 1.2-10.0 keV.

---

[1]XMM-Newton specifications are available at https://sci.esa.int/web/xmm-newton/

2.2.2   The High-Resolution Camera (HRC)

The *High-Resolution Camera (HRC)* is formed by two Micro-Channel Plates (MCP) with two detectors: HRC-I, intended for imaging, and HRC-S, made for spectroscopy. Each MCP is a 10 cm square cluster of lead-oxide glass tubes, with a diameter of $\sim 10\mu m$ and a length of 1.2 mm. The spectral resolution is negligible, so HRC must be combined together with the gratings. When it is used with the Low-Energy Transmission Grating (LETG) the resolution is improved up to 2000 in the soft X-ray energy range 0.08-2.0 keV. This configuration is used for high resolution spectroscopy of soft sources such as CVs.

2.2.3   The High-Resolution Spectrometers

X-rays reflected from the mirrors are intercept by two instruments specialized in high resolution spectroscopy: the *High Energy Transmission Grating Spectrometer (HETGS)* and the *Low Energy Transmission Grating Spectrometer (LETGS)*. These gratings are placed behind the mirrors and diffract the X-rays to one of the focal plane cameras. They allows investigation of temperature, ionization and chemical composition and provide detailed energy spectra distinguishing individual X-ray lines.

The LETG is a gold grating made of bars regular spaced with a period of $\sim 10\mu m$. In order to match Chandra mirrors, the gratings are installed onto a toroidal ring structure. The instrument is optimized over the energy bandwidth $\sim 0.09 - 4\,\mathrm{keV}$, corresponding to $3.1 - 138\,\text{Å}$, and has a resolving power ~ 1000 at 0.1 keV. The spectra of Nova YZ Ret were obtained with the particular combination HRC-I+LETG and the calibration was accessible only up to $71\,\text{Å}$.

The HETG consists of two arms: the *High-Energy Grating(HEG)*, with a period $\sim 2000\,\text{Å}$, and the *Medium-Energy Grating(MEG)*, with a period $\sim 4000\,\text{Å}$. HETG covers an energy range from 0.4 to 10 keV. HEG and MEG are oriented at slightly different angles so the X-rays are diffracted in a 'X' pattern at the focal plane. The gold coating of the gratings allows a more efficient diffraction, meaning that more X-rays are caught in the high resolution spectrum. [2]

---

[2]Detailed informations about the Chandra X-ray observatory can be found at https://chandra.harvard.edu/about/

2.3 Method of spectral analysis

I performed the spectral analysis on the Chandra and XMM X-rays data with `xspec` v12.12.1 package in `HEAsoft` v6.31.1. Various models were employed, including:

- `tbabs`, known as the Tuebingen-Boulder ISM absorption model, which incorporates absorption due to gas, grains, and molecules in the interstellar medium (ISM). It includes molecular hydrogen as a component and allows for variation in the equivalent hydrogen column density nh [66].

- `pcfabs`, or partial covering fraction absorption model, particularly useful in modeling Polars and IPs classes. It accounts for the additional absorption resulting from the accretion flow which partially cover the X-ray source. It features two free parameters: the equivalent hydrogen column density nh and the dimensionless covering fraction `CvrFract` [3].

- bbody representing a blackbody spectrum. It simulates emission from the WD atmosphere heated by accretion columns. Its parameters include the temperature kT in keV and the normalization constant `norm`, used to derive the bolometric blackbody luminosity when the source distance is known [4].

- apec, based on the Astrophysical Plasma Emission Code, which describes emission from a diffuse plasma in collisionally-ionization equilibrium using the `atomdb` code v3.0.9. It provides parameters such as plasma temperature kT in keV, redshift z, and normalization constant `norm` indicating emission measure. The vapec variant allows for modifications of He, C, N, O, Ne, Mg,Al, Si, S, Ar, Ca, Fe, Ni abundances relative to solar values, while the bvapec includes also the gaussian sigma for velocity broadening[67].

- The `powerlaw` model accounts for non-thermal cyclotron emission with a functional form of $A(E) = norm E^{-\alpha}$, where the photon index α and normalization constant $norm$ are

---

[3]For detailed model information, refer to https://heasarc.gsfc.nasa.gov/xanadu/xspec/manual/node263.html

[4]More information about the blackbody model can be found at https://heasarc.gsfc.nasa.gov/xanadu/xspec/manual/node136.html

input parameters [5].

- `agauss`, representing a simple gaussian profile, is essential fot fitting emission lines in high-resolution spectra [6].

- `redge`, which is useful to model the Recombination Radiation Continua (RRCs) in a Maxwell-Boltzmann distributed plasma, includes parameters such as the threshold energy and the plasma temperature [7].

---

[5]For specifications about the powerlaw model, visit https://heasarc.gsfc.nasa.gov/xanadu/xspec/manual/node221.html

[6]Informations about the agauss model are at https://heasarc.gsfc.nasa.gov/xanadu/xspec/manual/node131.html

[7]More informations about the redge model are available at https://heasarc.gsfc.nasa.gov/xanadu/xspec/manual/node224.html

Chapter 3

Nova V407 Lup

In this chapter, I discuss the X-ray and optical observations of Nova V407 Lup during its quiescent phase. The primary objective was to further investigate its magnetic nature, as it is identified as an IP candidate. The introductory paragraph provides an overview of the target's current understanding, followed by detailed spectral analyses conducted using data from the XMM-Newton EPIC cameras and RGS spectrometer (Sec.3.2). Concluding the chapter (Sec.3.4), I offer a brief discussion on the X-ray light curve and optical spectra analyses conducted by my collaborators.

3.1   Overview of the nova

Nova V407 Lup, also known as ASASSN-16kt, was initially detected during an outburst by the All-Sky Automated Survey for Supernovae (ASAS-SN) on 2016 September 24, at a magnitude of $V = 9.1$ [68]. The coordinates of this nova can be found in Tab.3.1. Since its discovery, various observations spanning optical, near-infrared, X-ray, and UV wavelengths have been conducted by instruments such as SALT, SMARTS, SOAR, Chandra, Swift, and XMM-Newton, starting from 2016 September 26. The nova reached its optical peak brightness of $V_{vis,max} = 5.60\,mag$ on September 26 2016, just 1.4 days after the initial eruption, with an impressive amplitude

Object	Right ascension (RA, J2000)	Declination (Dec, J2000)	Discovery date (UT)	Discovery V magnitude
Nova V407 Lup	$15^h29^m01.82^s$	$-44°49'40.89''$	2016-09-24.00	$9.1\,mag$

Table 3.1: Parameter of Nova V407 Lup

$\sim 15\,mag$. This rapid rise suggests a decline time $t_2 \leq 2.9\,days$, categorizing V407 Lup as a very fast nova [69]. Analysis of the Swift UV light curve revealed a periodicity of $3.57 \pm 0.0014\,hr$, correlating with the orbital period of the binary system. Furthermore, both Chandra and XMM-Newton light curves displayed peaks occurring at periods of approximately $565.04 \pm 0.68\,s$ and $564.96 \pm 0.50\,s$, respectively, indicating the spin period of the WD. These findings suggest the possible presence of a magnetized WD within the system [69].

Optical spectra obtained by Izzo et al. since day 5 post-outburst revealed dominant broad emission lines of Balmer, He I, and N III, accompanied by faint Fe II emission lines at various wavelengths. By day 19, prominent forbidden lines of O and N emerged, indicating the onset of the nebular phase. V407 Lup goes through the three main phases (see Sec.1.4) during the first three weeks [52, 70]. Later observations on days 164 and 209 show spectra dominated by broad nebular forbidden O lines, along with Balmer and forbidden Ne and Fe lines, confirming the nova's advancement into the nebular phase. The presence of Ne lines suggested a progenitor of a massive oxygen-neon (ONe) white dwarf [70]. Additionally, the detection of ^7Be, a precursor to ^7Li, indicated the capability of ONe novae to produce lithium, affirming CNe as significant contributors of stellar-origin lithium in the Galaxy [70].

Further spectral evolution on day 250 revealed the emergence of HeII and OVI lines, with HeII 4686 Å being the most prominent [52]. Evidence of accretion resumption was observed from day 325 onwards, indicated by both Swift and Chandra X-ray spectra. Swift observations revealed hard X-ray emissions above $\sim 1.5\,\mathrm{keV}$, while Chandra observations suggested a decrease in flux, possibly due to partial obscuration of the WD by an accretion disk [52].

Estimations place the mass of the WD between 1.1 and 1.3 $M_\odot$, as derived from t_2 and the peak temperature of the super-soft X-ray emission, approximately $80 \pm 10\,\mathrm{eV}$ [52].

Although the precise distance of Nova V407 Lup remains undetermined, Izzo et al. found $d = 10.9 \pm 1.6\,kpc$ using the MMRD method [70], while Gordon et al. estimated $d = 4.2 \pm 0.5\,kpc$ based on extinction and reddening maps [59]. GAIA parallax measurements for the progenitor candidate within 1 arcseconds from the nova position align with a geometric distance of $4.7^{+6.5}_{-2.5}\,kpc$ and a photogeometric distance of $8.6^{+4.4}_{-2.6}\,kpc$ [71].

3.2   The X-ray observations

Observations of Nova V407 Lup (PI: Marina Orio) were conducted using both the XMM-Newton EPIC cameras, operating in full window and imaging mode, and the RGS spectrometer. The observation period started on 26 February 2020, at 02:57 UT, with a total exposure duration of 48 ks. Within the $0.3 - 12\,\mathrm{keV}$ range, the MOS1 and MOS2 cameras recorded count rates of $0.039 \pm 0.0013\,cts\,s^{-1}$ and $0.0476 \pm 0.0014\,cts\,s^{-1}$, respectively. Additionally, the pn camera detected a count rate of $0.151 \pm 0.030\,cts\,s^{-1}$ in the $0.2 - 12\,\mathrm{keV}$ range. High-resolution spectra were obtained using the RGS spectrometer, covering the $5 - 35\text{Å}\,(0.35 - 2.48\,\mathrm{keV})$ range. The combined count rate from RGS1 and RGS2 exposures was measured at $0.0080 \pm 0.0008\,cts\,s^{-1}$ within the RGS range.

3.3   The X-ray spectral analysis

3.3.1   The EPIC spectra

In this analysis, I present three models utilized to fit the background-subtracted spectra of V407 Lup, extracted in the 0.3-10.0 keV range of the two MOS and in the 0.2-10.0 keV range of the pn. To enhance the signal-to-noise ratio and improve statistics, the spectra were binned with a minimum count requirement per energy bin. For MOS1 and MOS2, bins contained at least 50 counts, while for pn, the minimum count per bin was set to 60. In all models, a minimum column density of $N(H) \geq 0.14 \times 10^{22}\,cm^{-2}$ was assumed, based on the value provided by the `HEAsoft` tool nH[1], which indicated $N(H) \sim 0.154 \times 10^{22}\,cm^{-2}$.

Initially, I attempted to fit the spectra using a $TBabs \times pcfabs \times (apec + apec)$ model, denoted as *Model 1*. The best-fit parameters and plots are presented in Tab.3.2, in Fig.3.1, and fig.3.2 respectively. Two `apec` components were necessary to model the hardest and softest part of the spectra, with `pcfabs` utilized to account for additional absorption near the accretion poles in IPs. Notably, the covering fraction of `pcfabs` was very high, ranging from 41% to 48%. However, the temperature of the second `apec` component, which involves almost all the unabsorbed

---

[1]For further details, visit https://heasarc.gsfc.nasa.gov/cgi-bin/Tools/w3nh/w3nh.pl

flux, remained poorly constrained due to significant error bars, particularly when fitting MOS1 and MOS2 simultaneously.

Later, I explored *Model 2*, employing $TBabs \times (bb + pcfabs \times apec)$ combination. The best fit yielded a column density $N(H) = 11.46 \times 10^{22}\, cm^{-2}$ covering 45% of the space. The `blackbody` component aimed to model WD emission, but as we can see from Tab.3.3, its temperature is not consistent and exceeds the values for a WD, typically $\leq 90\,\mathrm{eV}$. Most of the unabsorbed flux is due to the `apec` component. The blackbody flux instead is only a small fraction with respect to the total, suggesting possible emission from a limited region, likely polar caps, rather than the entire WD surface. However, this model exhibited an unexplained soft excess in the pn spectrum as shown in Fig.3.3 and Fig.3.4.

Lastly, *Model 3*, namely $TBabs \times (powerlaw + vapec)$, was employed, combining a `vapec`, for the soft portion of the spectra, with a `powerlaw` component. The latter is sometimes necessary in fitting some X-ray spectra of IPs and involves the majority of the flux. It may indicate a non-thermal component probably due to synchrotron or cyclotron emission. A photon index $\alpha \simeq 1$ and a vapec temperature $kT_{vapec} \simeq 0.19\,\mathrm{keV}$ were derived for both pn and the combined instrument spectra. The other parameters are shown in Tab.3.4 while the plots are shown in Fig.3.5 and Fig.3.6. Considering possible differences in element abundances from solar values in novae, I varied C, N, Ne, Mg, and Fe abundances, assuming 1/10th of solar abundances as the minimum value. Fig.3.7 shows a *corner plot*, namely the 3 σ contours of the acceptable values varying two of the following parameters: N(H), photon index α, normalization of both components and `vapec` temperature with the `steppar` command. These four parameters are quite well constrained in a narrow range. Abundances are not shown in the corner plot since their determination has large errors due to limitations in resolving individual lines by EPIC cameras.

In conclusion the X-ray EPIC spectra of V407 Lup can be well fitted with both *Model 1* and *Model 3*, whereas *Model 2* must be rejected due to the presence of a soft excess in the pn spectrum.

Model 1: TBabs x pcfabs x (apec + apec)			
Parameter	MOS1+MOS2	PN	MOS1+MOS2+PN
$N(H) \times 10^{22}$ cm^{-2}	$0.19^{+0.12}_{-0.19}$	$0.14^{+0.05}_{-0.14}$	$0.15^{+0.06}_{-0.15}$
$N(H)^{a}_{pc} \times 10^{22}$ cm^{-2}	$22.68^{+57.07}_{-14.66}$	$4.69^{+3.05}_{-1.63}$	$8.24^{+5.46}_{-1.58}$
CvrFract ^{b}	$0.48^{+0.27}_{-0.15}$	$0.41^{+0.06}_{-0.15}$	$0.47^{+0.07}_{-0.12}$
$T_{apec,1}$(keV)	$0.17^{+0.05}_{-0.12}$	0.18 ± 0.02	0.17 ± 0.02
$T_{apec,2}$(keV)	≥ 64	$38.94^{+19.34}_{-4.59}$	$23.86^{+40.14}_{-10.48}$
$Norm_{apec,1} \times 10^{-4}$	$1.52^{+5.54}_{-1.13}$	$0.73^{+0.80}_{-0.22}$	$0.97^{+1.10}_{-0.36}$
$Norm_{apec,2} \times 10^{-4}$	$11.49^{+5.00}_{-1.88}$	$8.39^{+0.82}_{-0.65}$	$8.47^{+1.71}_{-0.79}$
$Flux^{c}_{total, abs} \times 10^{-12} \, erg \, cm^{-2} \, s^{-1}$	1.25	1.23	1.20
$Flux^{d}_{total, unabs} \times 10^{-12} \, erg \, cm^{-2} \, s^{-1}$	2.38	1.80	1.99
$Flux^{e}_{apec_1, abs} \times 10^{-12} \, erg \, cm^{-2} \, s^{-1}$	0.02	0.02	0.02
$Flux^{f}_{apec_2, abs} \times 10^{-12} \, erg \, cm^{-2} \, s^{-1}$	1.23	1.21	1.18
$Flux^{g}_{apec_1, unabs} \times 10^{-12} \, erg \, cm^{-2} \, s^{-1}$	0.35	0.17	0.23
$Flux^{h}_{apec_2, unabs} \times 10^{-12} \, erg \, cm^{-2} \, s^{-1}$	2.03	1.63	1.76
χ^2/d.o.f	1.12	1.62	1.39

Table 3.2: Best fit parameters of the $TBabs \times pcfabs \times (apec + apec)$ model. **Notes.** [a] N(H) of the partial covering absorber. [b] Covering fraction of the partial covering absorber. [c] The total absorbed X-Ray flux measured in the range 0.2-10.0 keV. [d] The unabsorbed X-Ray flux measured in the range 0.2-10.0 keV. [e] The absorbed X-Ray flux of the first apec component measured in the range 0.2-10.0 keV. [f] The absorbed X-Ray flux of the second apec component measured in the range 0.2-10.0 keV. [g] The unabsorbed X-Ray flux of the first apec component measured in the range 0.2-10.0 keV. [h] The unabsorbed X-Ray flux of the second apec component measured in the range 0.2-10.0 keV.
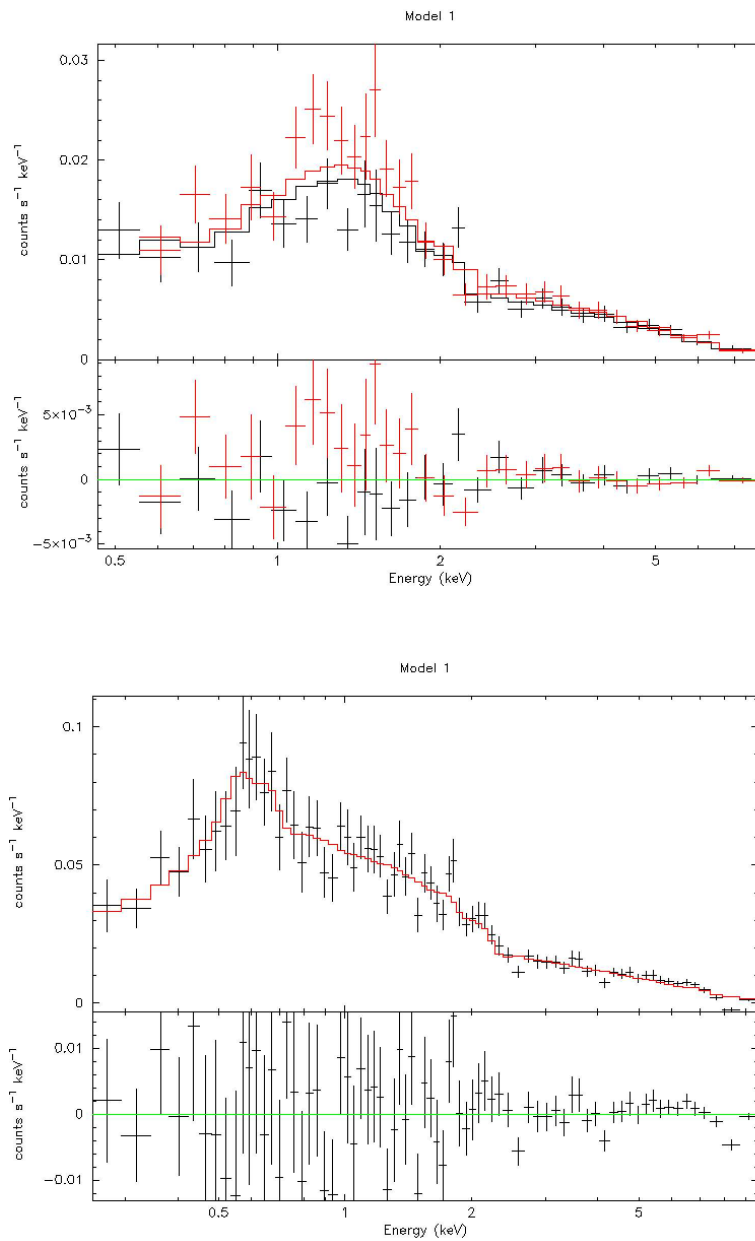
Figure 3.1: The upper panel shows the MOS1 and MOS2 spectra in black and red respectively. The solid lines represent the fit with *Model 1*. The lower panel displays the pn spectrum. Again, the solid lines indicate the fitting performed with *Model 1*. The x-axis scale is logarithmic.
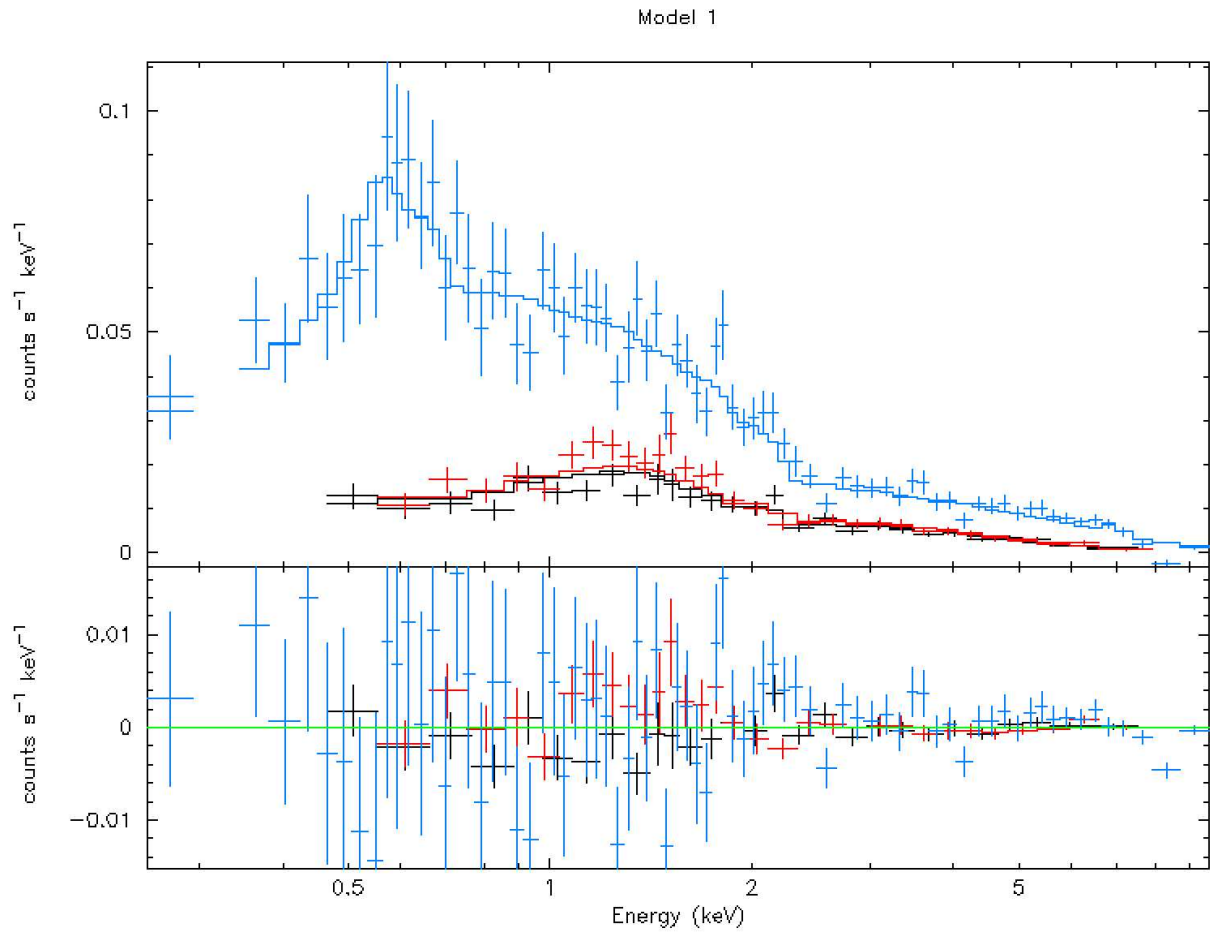
Figure 3.2: The three MOS1, MOS2 and pn spectra, respectively in red, black and blue. The solid lines indicate the fitting performed with *Model 1*. The x-axis scale is logarithmic.

Model 2: TBabs x (bb + pcfabs x apec)			
Parameter	MOS1+MOS2	PN	MOS1+MOS2+PN
N(H) $\times 10^{22}$ cm^{-2}	$0.22^{+0.13}_{-0.22}$	$0.30^{+0.11}_{-0.30}$	0.25 ± 0.10
N(H)$^a_{pc}\times 10^{22}$ cm^{-2}	$17.72^{+64.72}_{-9.80}$	$8.19^{+7.96}_{-4.20}$	$11.46^{+9.36}_{-4.63}$
CvrFract^b	$0.50^{+0.25}_{-0.17}$	0.43 ± 0.12	$0.45^{+0.07}_{-0.09}$
T$_{bb}$(eV)	≥ 90	≥ 90	≥ 90
T$_{apec}$(keV)	≥ 25.41	$16.23^{+23.47}_{-4.58}$	$19.62^{+21.36}_{-7.19}$
Norm$_{bb}\times 10^{-6}$	$6.64^{+13.49}_{-4.92}$	$11.99^{+18.39}_{-10.77}$	$7.21^{+11.45}_{-5.32}$
Norm$_{apec}$ $\times 10^{-6}$	$980.1^{+547.3}_{-207.4}$	$846.3^{+112.82}_{-84.84}$	$880.1^{+130.55}_{-85.88}$
Flux$^c_{total,abs}$ $\times 10^{-12}$ $erg\,cm^{-2}\,s^{-1}$	1.22	1.21	1.21
Flux$^d_{total,unabs}$ $\times 10^{-12}$ $erg\,cm^{-2}\,s^{-1}$	2.26	2.59	2.33
Flux$^e_{bb,abs}$ $\times 10^{-12}$ $erg\,cm^{-2}\,s^{-1}$	0.03	0.04	0.04
Flux$^f_{bb,unabs}$ $\times 10^{-12}$ $erg\,cm^{-2}\,s^{-1}$	0.28	0.78	0.47
Flux$^g_{apec,abs}$ $\times 10^{-12}$ $erg\,cm^{-2}\,s^{-1}$	1.19	1.17	1.17
Flux$^h_{apec,unabs}$ $\times 10^{-12}$ $erg\,cm^{-2}\,s^{-1}$	1.98	1.81	1.86
χ^2/d.o.f.	1.12	1.80	1.48

Table 3.3: Best fit parameters of the $TBabs \times (bb + pcfabs \times apec)$ model. **Notes.** [a] N(H) of the partially covering absorber. [b] Covering fraction of the partially covering absorber. [c] Total absorbed flux in the 0.2-10.0 keV range. [d] Total unabsorbed flux in the 0.2-10.0 keV. range [e] Absorbed flux of the blackbody component in the 0.2-10.0 keV range. [f] Unabsorbed flux of the blackbody component in the 0.2-10.0 keV range. [g] Absorbed flux of the apec component in the 0.2-10.0 keV. [h] Unabsorbed flux of the apec component in the 0.2-10.0 keV
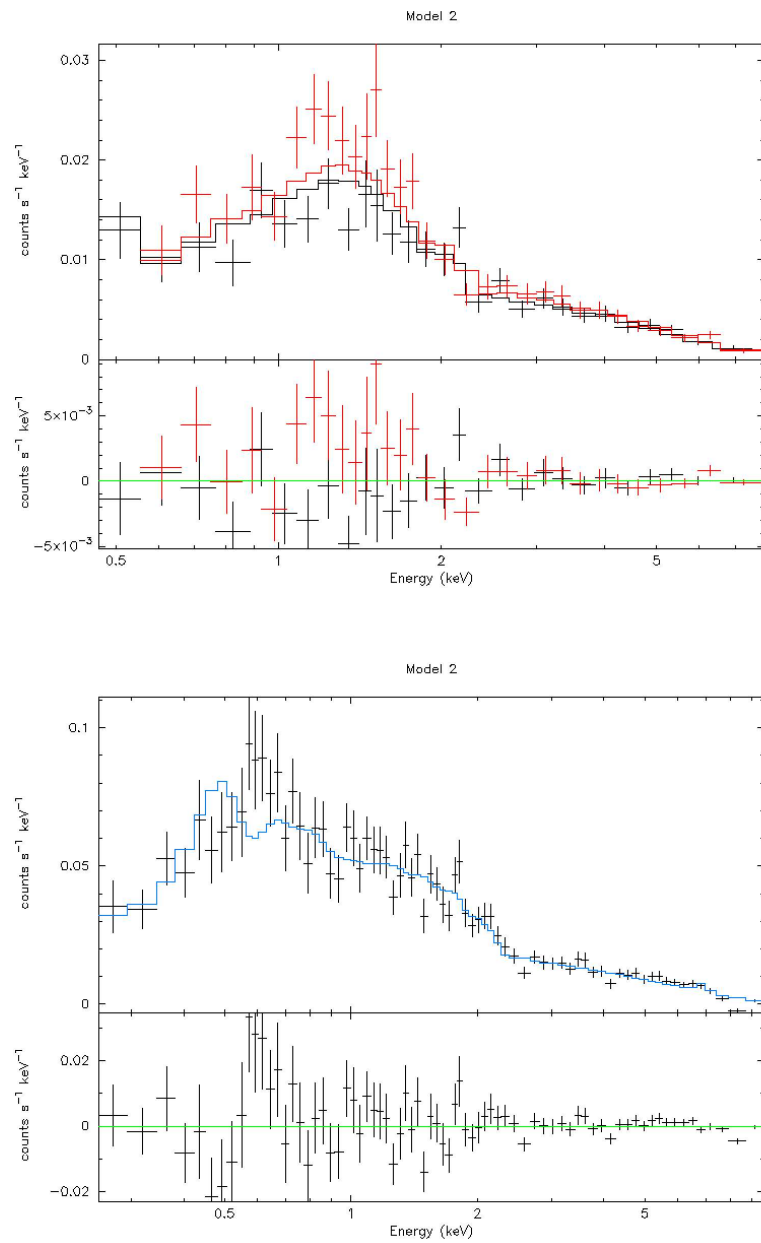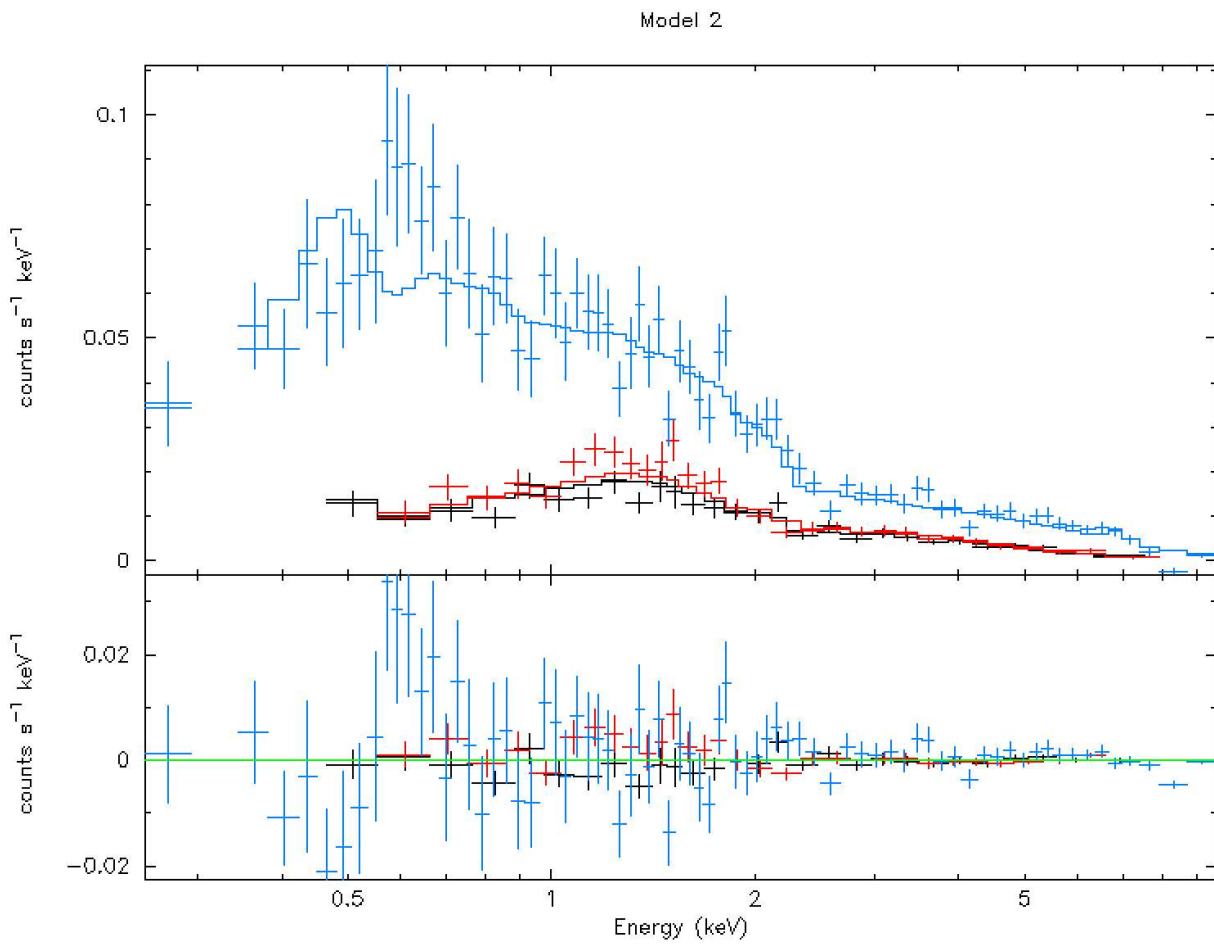
Figure 3.3: The upper panel shows the MOS1 and MOS2 spectra in black and red respectively. The solid lines represent the fit with *Model 2*. The lower panel displays the pn spectrum. Again, the solid lines indicate the fitting performed with *Model 2*. The x-axis scale is logarithmic.

Figure 3.4: The three MOS1, MOS2 and pn spectra, respectively in red, black and blue. The solid lines indicate the fitting performed with *Model 2*. The x-axis scale is logarithmic.

Model 3: TBabs x (powerlaw + vapec)		
Parameter	PN	MOS1+MOS2+PN
$N(H) \times 10^{22} \, cm^{-2}$	$0.16^{+0.17}_{-0.16}$	$0.14^{+0.08}_{-0.14}$
PhoIndex(α)[a]	$1.02^{+0.19}_{-0.08}$	$0.99^{+0.07}_{-0.05}$
$Norm_{pow} \times 10^{-5}$	$8.83^{+2.65}_{-0.99}$	$8.32^{+0.88}_{-0.45}$
$T_{vapec}(keV)$	$0.19^{+0.06}_{-0.03}$	$0.19^{+0.08}_{-0.04}$
$Norm_{vapec} \times 10^{-5}$	$5.28^{+137.5}_{-3.35}$	$4.12^{+5.10}_{-1.33}$
C	$6.78^{+80.01}_{-6.78}$	$8.23^{+25.27}_{-8.23}$
N	$0.77^{+6.44}_{-0.77}$	$1.15^{+7.49}_{-1.15}$
Ne	$0.10^{+1.83}_{-0.10}$	$0.51^{+2.10}_{-0.51}$
Mg	≤ 0.1	≤ 0.1
Fe	$1.44^{+14.98}_{-1.44}$	$1.05^{+16.41}_{-1.05}$
Flux$^b_{total,abs} \times 10^{-12} \, erg \, cm^{-2} \, s^{-1}$	1.26	1.25
Flux$^c_{total,unabs} \times 10^{-12} \, erg \, cm^{-2} \, s^{-1}$	1.51	1.45
Flux$^d_{pow,abs} \times 10^{-12} \, erg \, cm^{-2} \, s^{-1}$	1.23	1.22
Flux$^e_{pow,unabs} \times 10^{-12} \, erg \, cm^{-2} \, s^{-1}$	1.35	1.32
Flux$^f_{vapec,abs} \times 10^{-12} \, erg \, cm^{-2} \, s^{-1}$	0.03	0.03
Flux$^g_{vapec,unabs} \times 10^{-12} \, erg \, cm^{-2} \, s^{-1}$	0.16	0.13
χ^2/d.o.f.	1.86	1.51

Table 3.4: Best fit parameters of the $TBabs \times (powerlaw + vapec)$ model. **Notes.** [a] Photon index of power law (dimensionless). [b] Total absorbed X-Ray flux in the 0.2-10.0 keV range. [c] Total unabsorbed flux in the 0.2-10.0 keV range. [d] Absorbed flux of the powerlaw component in the 0.2-10.0 keV range . [e] Unabsorbed flux of the powerlaw component in the 0.2-10.0 keV range. [f] Absorbed flux of the vapec component in the 0.2-10.0 keV range. [g] Unabsorbed flux of the vapec component in the 0.2-10.0 keV range.
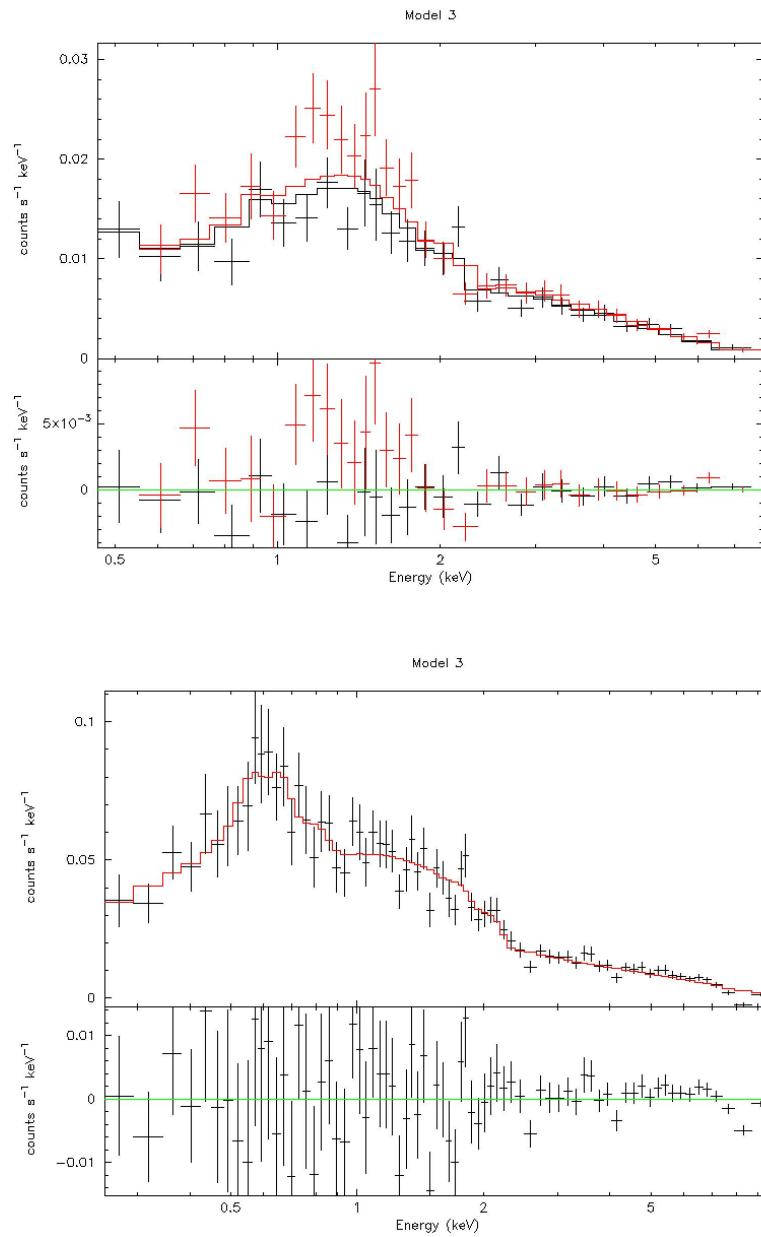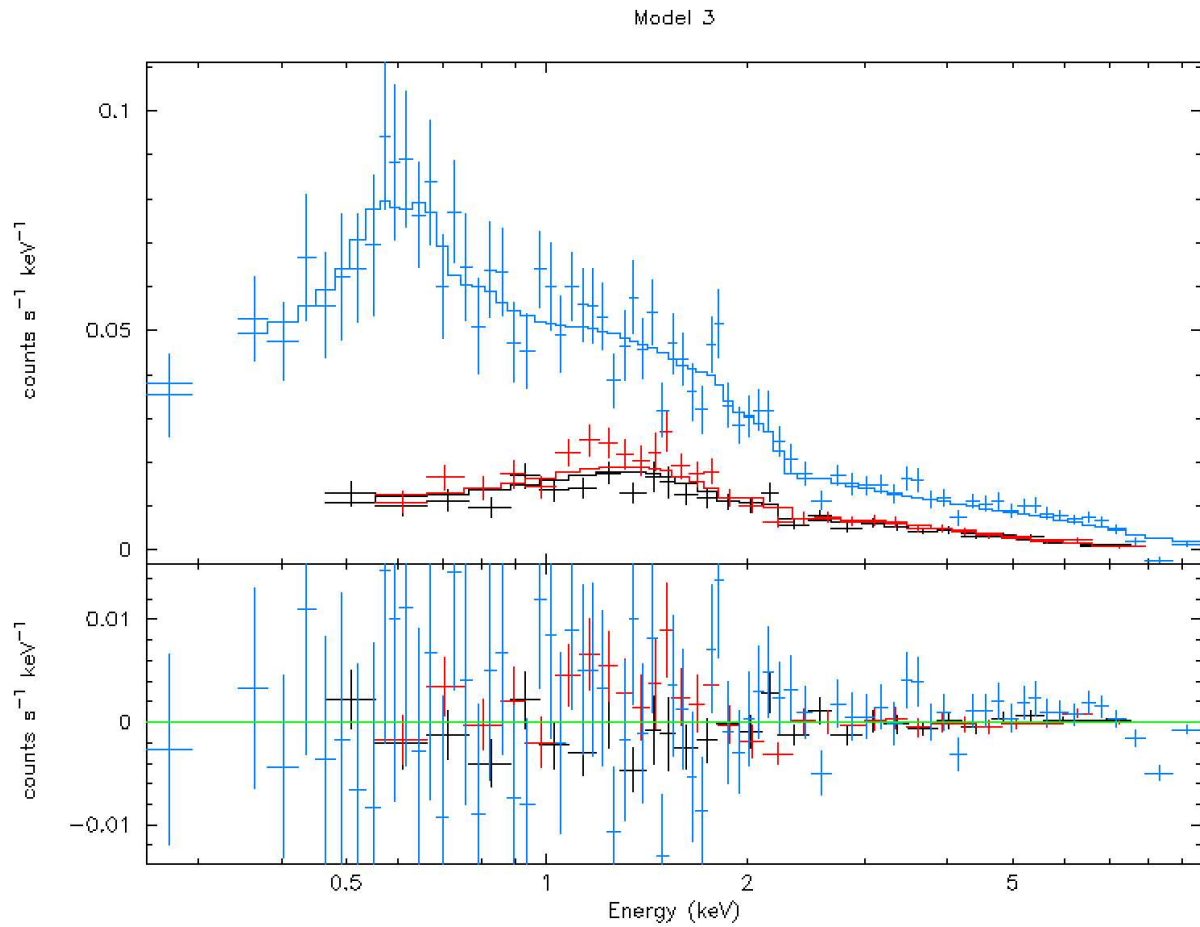
Figure 3.5: The upper panel shows the MOS1 and MOS2 spectra in black and red respectively. The solid lines represent the fit with *Model 3*. The lower panel displays the pn spectrum. Again, the solid lines indicate the fitting performed with *Model 3*. The x-axis scale is logarithmic.

Figure 3.6: The three MOS1, MOS2 and pn spectra, respectively in red, black and blue. The solid lines indicate the fitting performed with *Model 3*. The x-axis scale is logarithmic.
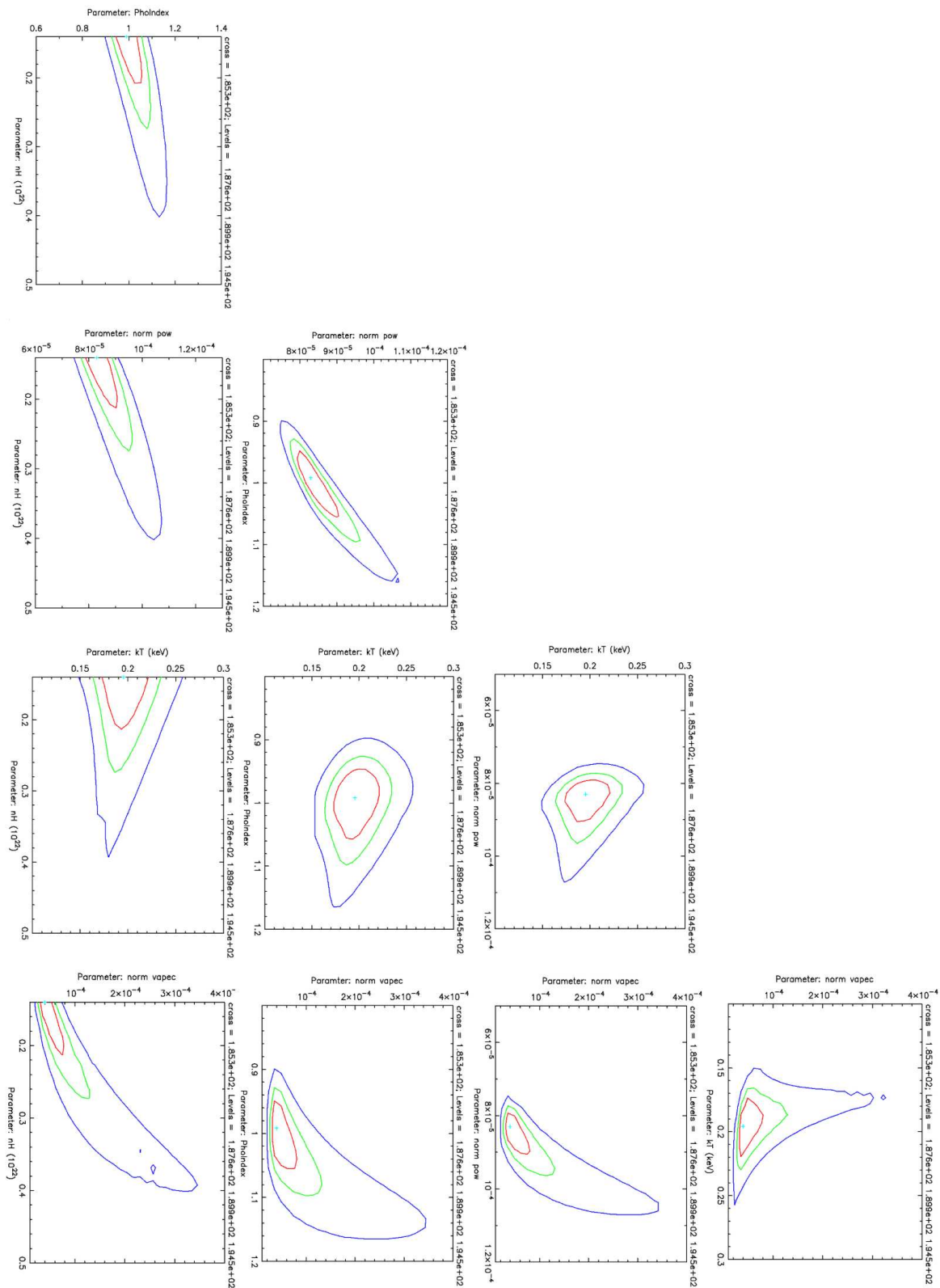
Figure 3.7: Contours plots of *Model3*. The red, green and blue solid lines correspond respectively to the 68%, 90% and 99% confidence levels.

3.3.2 The RGS spectrum

I conducted the RGS analysis by simultaneously utilizing both the first (RGS1) and second-order (RGS2) spectra, which were then coadded. They are respectively denoted as RGS1 + RGS2 and RGS. To improve the signal-to-noise ratio and thus better statistics, all the spectra were binned with a minimum of 10 counts per energy bin.

Initially, I attempted to model the RGS using *Model A*, comprising a combination of a `blackbody` and a `vapec` component, expressed as $Tbabs \times (bb + vapec)$. The best-fit parameters revealed a blackbody temperature T_{bb} of approximately 42.52 eV and a vapec temperature T_{vapec} of roughly 1.30 keV. Predominantly, the flux arise from the blackbody, with all abundances enhanced relative to solar values, as detailed in Tab.3.5. However, the fit was not rigorous, evident from Fig.3.8, with a $\chi^2 < 1$ due to the RGS spectrum's low signal-to-noise ratio. Consequently, abundance error bars could not be accurately determined. Tab.3.7 and Tab.3.8, along with Fig.3.10, present the identification of spectral lines using the `atomDB` v3.0.9 database[2]. This classification contributes in understanding the distribution of elements across the RGS energy range. Slight discrepancies in identification arise when plotting RGS1 and RGS2 simultaneously or when coadded, attributable to differing signal-to-noise ratios. However, the RGS classification holds greater reliability.

An improved fit was achieved with *Model B*, featuring two `vapec` components to cover both the softer and harder portions of the spectrum. The best-fit parameters and plots are detailed in Tab.3.6 and Fig.3.9, indicating vapec temperatures of 1.25 and 0.24 keV, respectively. While the RGS lacks sensitivity to the hard spectrum, it does reveal that emission lines, if attributed to collisional ionization equilibrium thermal components, originate from regions with varied temperatures, even in the lower energy range. Notably, the Na X line at 11.191 Å couldn't be fitted due to the limitation of `apec` which includes only solar abundances of sodium. However, allowing other elements to vary resulted in all elements being enhanced relative to solar abundances, except for Mg, which exhibited strong depletion, and Fe and N, which mirrored solar abundances. Unfortunately, achieving a statistically significant fit together with the EPIC cameras was not possible due to the low signal-to-noise ratio.

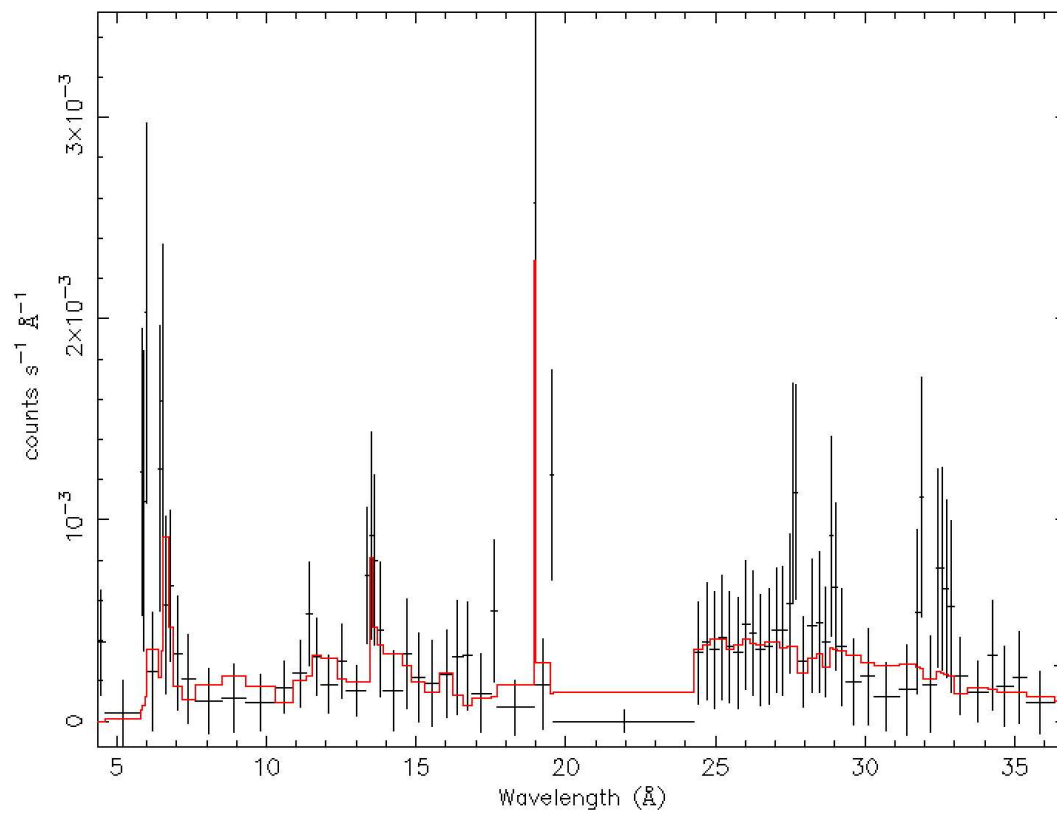[2]For more information, visit `http://www.atomdb.org/Webguide/webguide.php`

Figure 3.8: The black dots represents the coadded RGS1 and RGS2 spectra within the 5-35 Å range, while the solid red line shows the fit with *Model A*.

Model A: TBabs x (bb + vapec)	
Parameter	RGS
N(H)$\times 10^{22}$ cm^{-2}	$0.14^{+0.10}_{-0.14}$
T$_{bb}$(eV)	$42.52^{+7.27}_{-6.70}$
Norm$_{bb}\times 10^{-4}$	$14.08^{+14.59}_{-3.47}$
T$_{vapec}$(keV)	$1.30^{+0.36}_{-0.23}$
Norm$_{vapec}\times 10^{-4}$	$2.46^{+11.11}_{-1.28}$
C	74.16
N	5.78
O	7.35
Si	19.97
Fe	3.02
Flux$^a_{total,abs}$ $\times 10^{-12}$ $erg\,cm^{-2}\,s^{-1}$	1.86
Flux$^b_{total,unabs}$ $\times 10^{-12}$ $erg\,cm^{-2}\,s^{-1}$	5.65
Flux$^c_{bb,abs}$ $\times 10^{-12}$ $erg\,cm^{-2}\,s^{-1}$	0.67
Flux$^d_{bb,unabs}$ $\times 10^{-12}$ $erg\,cm^{-2}\,s^{-1}$	3.95
Flux$^e_{vapec,abs}$ $\times 10^{-12}$ $erg\,cm^{-2}\,s^{-1}$	1.19
Flux$^f_{vapec,unabs}$ $\times 10^{-12}$ $erg\,cm^{-2}\,s^{-1}$	1.70
χ^2/d.o.f.	0.81

Table 3.5: Best fit parameters of the $TBabs \times (bb + vapec)$ model. **Notes.** [a] Total absorbed X-Ray flux in the 0.35-2.48 keV range. [b] Total unabsorbed flux in the 0.35-2.48 keV range. [c] Absorbed flux of the blackbody component in the 0.35-2.48 keV range . [d] Unabsorbed flux of the blackbody component in the 0.35-2.48 keV range. [e] Absorbed flux of the vapec component in the 0.35-2.48 keV range. [f] Unabsorbed flux of the vapec component in the 0.35-2.48 keV range.

Model B: TBabs x (vapec + vapec)	
Parameter	RGS
N(H)$\times 10^{22}$ cm^{-2}	$0.14^{+0.07}_{-0.14}$
$T_{\mathrm{vapec},1}$(keV)	$1.25^{+0.28}_{-0.11}$
Norm$_{\mathrm{vapec},\,1}\times 10^{-5}$	$8.13^{+75.82}_{-7.27}$
$T_{\mathrm{vapec},\,2}$(keV)	$0.24^{+0.04}_{-0.03}$
Norm$_{\mathrm{vapec},\,2}\times 10^{-5}$	$18.82^{+201.03}_{-19.54}$
C	17.37
N	1.08
O	0.77
Ne	3.67
Mg	≤ 0.1
Al	≥ 100
Si	54.85
S	94.42
Ar	73.98
Ca	71.22
Fe	1.04
Ni	≥ 100
Flux$^a_{total,abs}$ $\times 10^{-12}$ $erg\,cm^{-2}\,s^{-1}$	1.89
Flux$^b_{total,unabs}$ $\times 10^{-12}$ $erg\,cm^{-2}\,s^{-1}$	5.00
Flux$^c_{vapec_1,abs}$ $\times 10^{-12}$ $erg\,cm^{-2}\,s^{-1}$	1.11
Flux$^d_{vapec_1,unabs}$ $\times 10^{-12}$ $erg\,cm^{-2}\,s^{-1}$	0.78
Flux$^e_{vapec_2,abs}$ $\times 10^{-12}$ $erg\,cm^{-2}\,s^{-1}$	3.58
Flux$^f_{vapec_2,unabs}$ $\times 10^{-12}$ $erg\,cm^{-2}\,s^{-1}$	1.42
χ^2/d.o.f.	0.95

Table 3.6: Best fit parameters of the $TBabs \times (bb + vapec)$ model. **Notes.** [a] Total absorbed X-Ray flux in the 0.35-2.48 keV range. [b] Total unabsorbed flux in the 0.35-2.48 keV range. [c] Absorbed flux of the blackbody component in the 0.35-2.48 keV range . [d] Unabsorbed flux of the blackbody component in the 0.35-2.48 keV range. [e] Absorbed flux of the vapec component in the 0.35-2.48 keV range. [f] Unabsorbed flux of the vapec component in the 0.35-2.48 keV range.
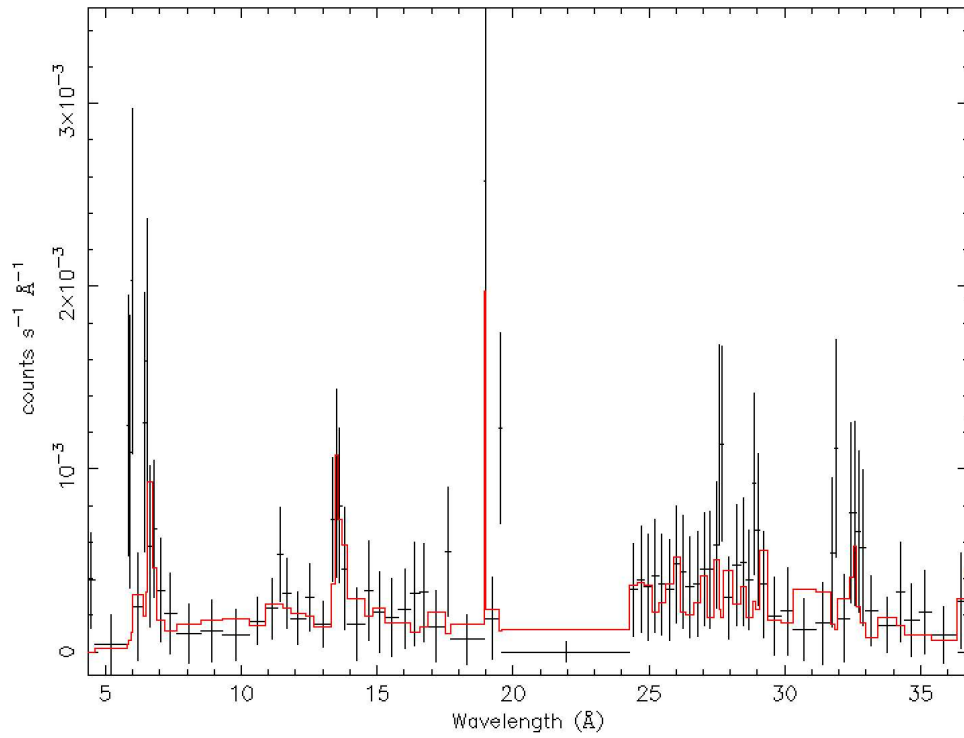
Figure 3.9: The black dots represents the coadded RGS1 and RGS2 spectra within the 5-35 Å range, while the solid red line shows the fit with *Model B*.

RGS1 + RGS2	
Line	Wavelength (Å)
Si XIV	6.180
Ne IX	11.547
Ne IX	13.447
N VI	24.962
C VI	28.466
N VI	28.780
C VI	33.734

Table 3.7: Spectral lines identification of the first and second order spectra plot simultaneously.

RGS	
Line	Wavelength (Å)
Si XIV	6.180
Si XIII	6.648
Na X	11.191
Fe XIX	13.518
O VII	18.932
N VI	28.787
Fe XVII	31.878
Ca XII	33.014

Table 3.8: Spectral lines identification of the coadded RGS1 and RGS2 spectra
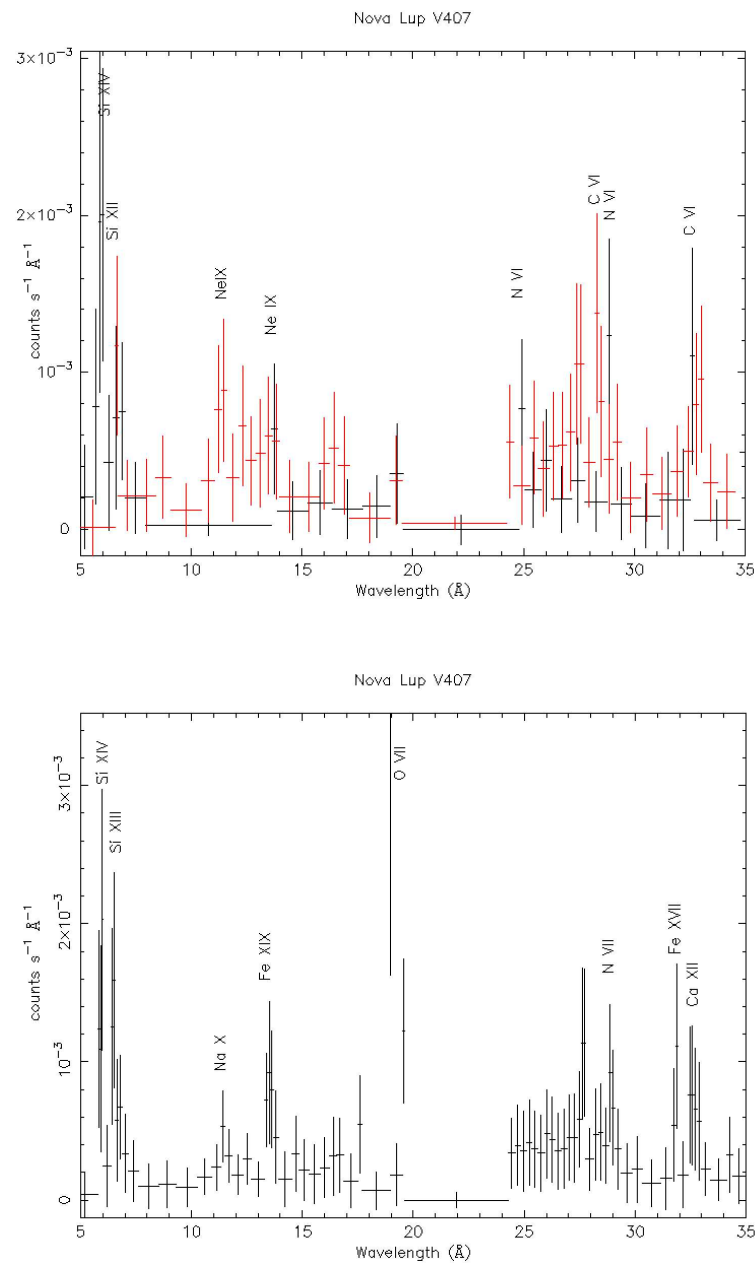
Figure 3.10: The upper panel shows the spectral lines identification when the RGS1 and RGS2 spectra, outlined in black and red respectively, are plotted together. The bottom panel illustrates the classification of the coadded RGS spectrum.

3.4   Work done by my collaborators

In the following sections (Sec. 3.4.1 and Sec. 3.4.2), I provide a concise overview of the timing and optical spectra analyses performed by my collaborators.

3.4.1   The timing analysis

The Lombe-Scargle algorithm

The Lomb-Scargle algorithm is a method for detecting periodic signals in unevenly spaced time-series data, particularly useful in in X-ray light curves. Given a set of observations (t_i, x_i), where x_i is measured at a set of time t_i, the Lombe-Scargle periodogram P_ω at angular frequency ω is defined as:

$$P(\omega) = \frac{1}{2} \left[\frac{\left(\sum_i y_i \cos \omega(t_i - \tau) \right)^2}{\sum_i \cos^2 \omega(t_i - \tau)} + \frac{\left(\sum_i y_i \sin \omega(t_i - \tau) \right)^2}{\sum_i \sin^2 \omega(t_i - \tau)} \right] \tag{3.1}$$

where τ is a phase offset introduced to account for the uneven spacing of the time series data. It is defined as:

$$\tan(2\omega\tau) = \frac{\sum_i \sin 2\omega t_i}{\sum_i \cos 2\omega t_i} \tag{3.2}$$

It ensures that the periodic signal is accurately detected even with irregular sampling [72]. The periodogram is used because, if the sample x_i contains a sinusoidal component with frequency ω_0, the sine and cosine functions at and near $\omega = \omega_0$ are in phase, making a larger contribution to the sums in Eq.3.1.

The analysis of the light curve

The timing analysis is a key point to confirm the magnetic nature of Nova V407 Lup. It was performed by Martin Melicherčík, using the Lombe-Scargle algorithm (see above)[3]. The light curves and background were extracted from a circular region, with a radius of 15", centered and offset relative to the source, respectively. Consistent with the X-ray analysis, the binning for MOS1, MOS2, and pn was maintained, with the exclusion of the last 4.5 ks region across all instruments due to increased background levels. The analysis revealed a periodicity of $565.64\,s$,

---

[3]They used the python's package `Astropy` [73, 74, 75]

as shown in Fig. 3.11, with varying confidence levels: 99.9 % for pn, 93 % for MOS1, and 34 % for MOS2. To determine the statistical error of the pn, a Gaussian function was fitted to its peak, yielding a sigma error parameter of approximately $3.10\,s$. Recognizing the dependency of this error on the periodogram resolution, further estimations were conducted through simulations. By fitting a sine function to the pn light curve with the periodicity fixed at $565.64\,s$, simulations of ten thousand light curves with added Poisson noise was performed. From these simulations, the periodogram was calculated for each and identified the peak periodicity. Subsequently, the resulting histogram of periodicities was fitted with a Gaussian function, yielding a value for the statistical uncertainty of $\sigma = 0.33$. Thus, the period with a 1σ error is $565.68 \pm 0.33\,s$. Similar analyses were conducted for MOS1 and MOS2, yielding respective results of $566.18 \pm 0.81\,s$ and $564.36 \pm 0.92\,s$. Despite the lower confidence level obtained with the MOS1 data, the consistency among the three periods is evident. The highly significant pn result, together with its robust confidence level, supports the definitive presence of periodic modulation in the X-ray light curve.
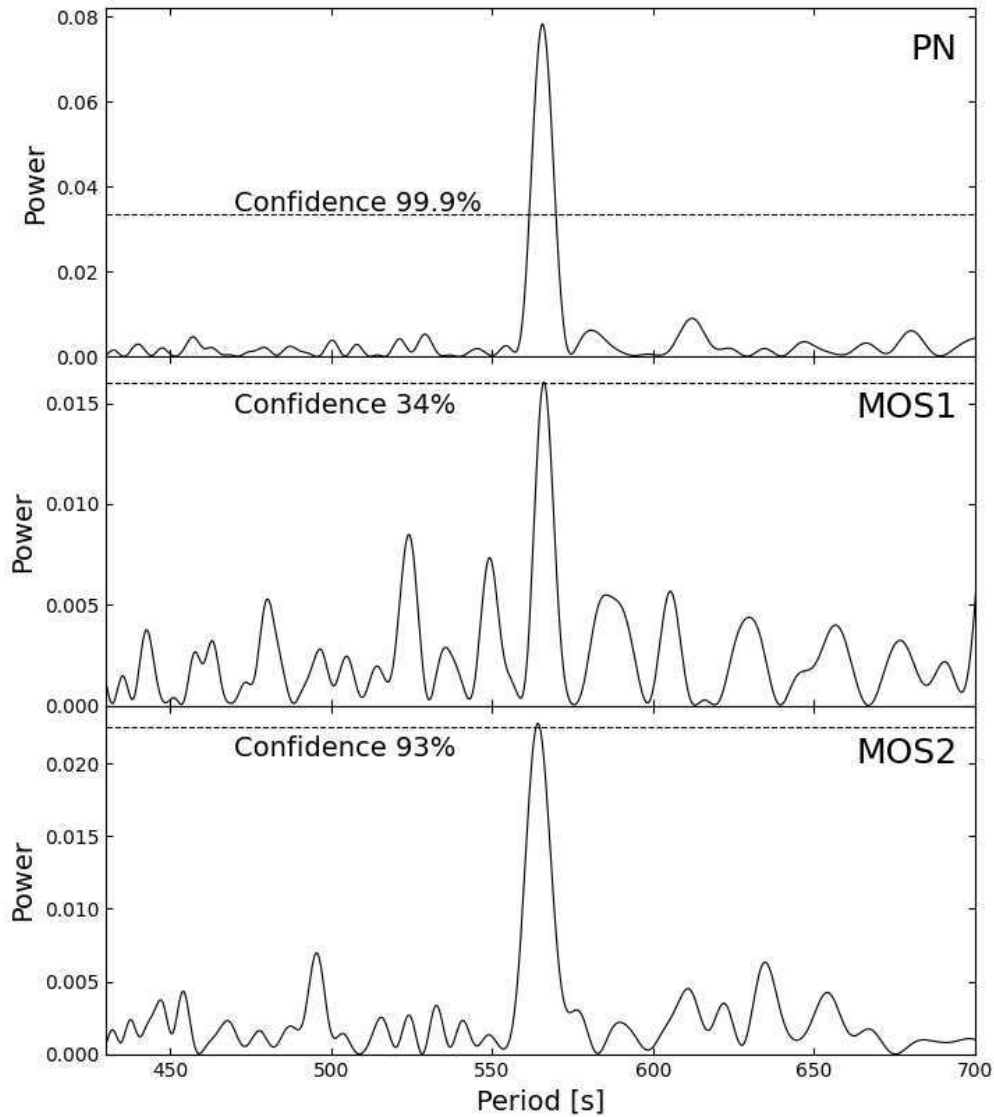
Figure 3.11: Periodograms calculated from all three X-ray light curves from XMM.The power of a peak at the 90%, 99% and 99.9% confidence levels is indicated by the red horizontal lines.

3.4.2   The optical spectra analysis

Observations of Nova V407 Lup were conducted using the High Resolution Spectrograph (HRS) at the South African Large Telescope (SALT) in the optical range spanning $3700 - 8900\,\text{Å}$. The telescope operated at a low-resolution mode, specifically with a resolving power of $R \sim 14.000$. These observations were distributed across five epochs: four occurred between 2019 February 22 and 2019 March 27, with the final epoch on 2022 May 10. Spectral analysis and line classification, as shown in Fig.3.12 and Fig.3.13, were conducted using IRAF v 2.16.1 by Dr. Stefano Ciroi. Throughout all epochs, prominent emission Balmer lines were observed alongside the Bowen fluorescence, occasionally found in magnetic systems [76], and the He II lines at 4541, 5411, and 4685.7Å. These He II lines exhibit high ionization potentials, with a transition occurring at $54.4\,\text{eV}$. However, as illustrated in Tab.3.9, the [O III] and [N II] nebular lines were not detected in the 2022 observations. This suggests the presence of nebular emission for at least 2.5 years following the nova outburst, which ceased after 5.5 years. Due to the non available absolute flux calibration, only the level above the continuum and the equivalent width (EW) could be used for line analysis. The EW of He II and Hα exhibited variability within the measurement errors, with no observable intensity decline between 2019 and 2022. However, the He II $5411\,\text{Å}$ line exhibited fluctuations across the five epochs, potentially indicating multiple components within it.

Table 3.9: The table shows the nominal and measured wavelength of each line, the continuum flux level assumed under each line, the flux in the line above the assumed continuum level, the root mean square of the flux to indicate the noise level, the equivalent width with its error, the height of the Gaussian and of the Lorentzian functions, the equivalent widths of the Gaussian and of the Lorentzian.

| Line	Lambda(Å)	Center(Å)	Continuum	Rms$_{cont}$	Line Flux	Eqw	Core	Gfwhm	Lfwhm
	(Å)	(Å)	($erg/cm^2/s/Å$)	($erg/cm^2/s$)	($erg/cm^2/s/Å$)	(Å)	($erg/cm^2/s/Å$)	(Å)	(Å)
				2019/02/22					
HeII	4685.7	4684.191	2.956×10^{-16}	7.406×10^{-18}	2.818×10^{-15}	9.535 ± 0.754	1.371×10^{-16}	–	–
[O III]	4958.9	4955.757	2.740×10^{-16}	6.044×10^{-18}	1.953×10^{-15}	7.128 ± 1.111	4.518×10^{-17}	40.61	–
[O III]	5006.8	5006.914	2.714×10^{-16}	6.044×10^{-18}	5.631×10^{-15}	20.75 ± 1.42	1.303×10^{-17}	40.61	–
Hα	6562.8	6560.505	1.603×10^{-16}	3.322×10^{-18}	6.124×10^{-15}	38.22 ± 1.48	1.856×10^{-16}	–	21.01
				2019/03/15					
HeII	4685.7	4684.316	2.282×10^{-16}	2.667×10^{-18}	2.236×10^{-15}	9.797 ± 0.364	1.046×10^{-16}	–	13.61
[O III]	4958.9	4950.532	2.122×10^{-16}	2.667×10^{-18}	1.795×10^{-15}	8.459 ± 0.680	3.932×10^{-17}	42.89	–
[O III]	5006.8	5006.359	2.095×10^{-16}	2.667×10^{-18}	4.709×10^{-15}	22.48 ± 0.87	1.031×10^{-16}	42.89	–
Hα	6562.8	6562.778	1.230×10^{-16}	2.708×10^{-18}	5.983×10^{-15}	48.65 ± 1.90	1.582×10^{-16}	–	24.08
				2019/03/16					
HeII	4685.7	4684.016	2.945×10^{-16}	6.601×10^{-18}	1.390×10^{-15}	4.718 ± 0.420	9.900×10^{-17}	13.19	–
[O III]	4958.9	4950.532	2.122×10^{-16}	2.667×10^{-18}	1.795×10^{-15}	8.459 ± 0.680	3.932×10^{-17}	42.89	–
[O III]	5006.8	5006.359	2.095×10^{-16}	2.667×10^{-18}	4.709×10^{-15}	22.48 ± 0.87	1.031×10^{-16}	42.89	–
Hα	6562.8	6562.778	1.230×10^{-16}	2.708×10^{-18}	5.983×10^{-15}	48.65 ± 1.90	1.582×10^{-16}	–	24.08
				2019/03/27					
HeII	4685.7	4683.656	2.605×10^{-16}	2.999×10^{-18}	1.205×10^{-15}	4.624 ± 0.204	9.228×10^{-17}	12.26	–
[O III]	4958.9	4951.589	2.436×10^{-16}	2.999×10^{-18}	1.309×10^{-15}	5.371 ± 0.638	2.819×10^{-17}	43.61	–
[O III]	5006.8	5005.869	2.394×10^{-16}	2.999×10^{-18}	3.693×10^{-15}	15.43 ± 0.78	7.955×10^{-17}	43.61	–
Hα	6562.8	6561.745	1.345×10^{-16}	2.114×10^{-18}	3.055×10^{-15}	22.7 ± 0.7	1.224×10^{-16}	23.45	–
				2022/05/10					
HeII	4685.7	4686.365	6.932×10^{-17}	2.272×10^{-18}	6.108×10^{-16}	8.811 ± 0.851	3.558×10^{-17}	16.13	–
Hα	6562.8	6560.052	4.716×10^{-17}	1.531×10^{-18}	1.335×10^{-15}	28.3 ± 2.248	3.260×10^{-17}	–	26.07
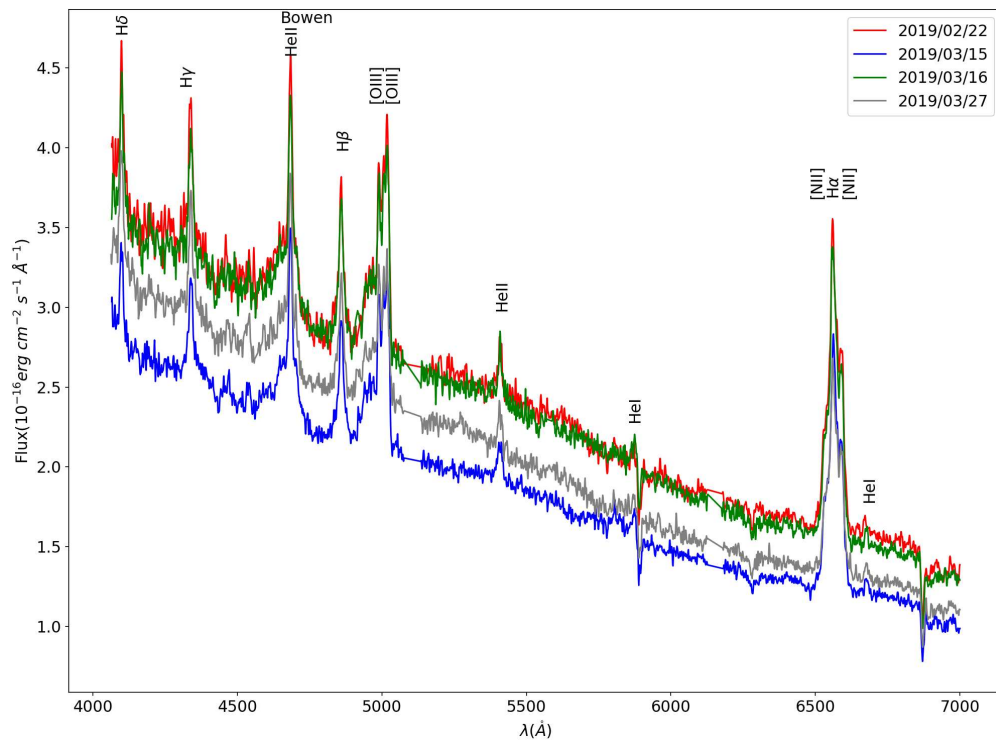
Figure 3.12: The non-dereddened optical spectra of Nova V407 Lup taken in 2019 during the first 4 epochs. The flux is in arbitrary unity and the spectra are shifted for clarity.
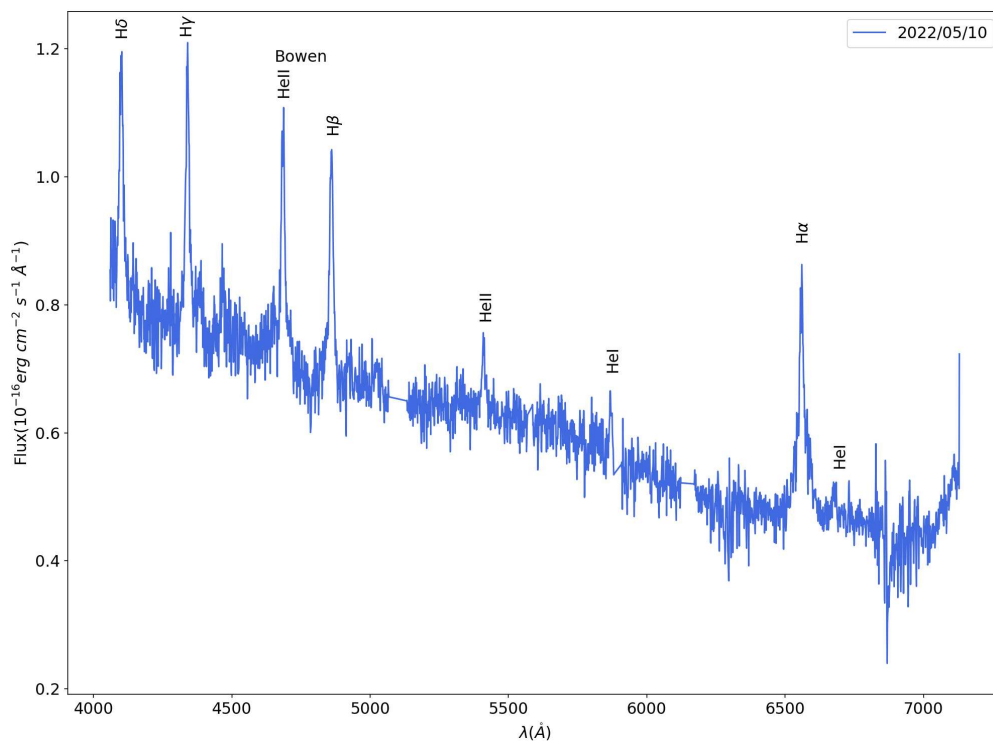

Figure 3.13: The non-dereddened optical spectrum of Nova V407 Lup taken in 2022 during the last epoch.

3.5 Discussion

Observations conducted during the resumption of quiescent accretion have confirmed Nova V407 Lup as an Intermediate Polar. A supersoft component, observed 3.5 years post-outburst, can be modeled with a thermal plasma ranging from $150 - 200\,\mathrm{eV}$, suggesting an origin different from residual nuclear burning. Furthermore, the detection of several prominent lines in the low signal-to-noise ratio RGS spectrum implies the soft spectrum may comprise multiple components. The identification of the hardest component of the spectrum, fitted with a powerlaw, raises the possibility of V407 Lup being a WD pulsar like AR Sco [77] or the WD in J191213.72 - 441045.1 [78]. In such a scenario, the strong magnetic field of the WD could accelerate particles from the companion's atmosphere, potentially generating non-thermal synchrotron emission. However, this remains speculative, and further observation is required for clarification. The detection of periodic modulation at $565.64\,s$, aligned with the WD's spin period, underlines its binary IP nature. Optical spectra prove the presence of a highly energetic photoionizing source even 5.5 years post-outburst. However, the disappearance of [O III] lines between 2019 and 2022 indicates significant dispersion of the nebula, probably started 2.5 years after the outburst.

Chapter 4

Nova YZ Ret 2020

This chapter focuses on Nova YZ Ret 2020. Section 4.1 presents the current understanding of the nova. In Section 4.3, I present the analysis conducted on the XMM RGS and the the Chandra LEGTS spectrum. Finally, Section 4.2 highlights the key findings from the density diagnostics performed by my collaborators.

4.1 The nova outburst

The nova was discovered in outburst at 5th magnitude on 2020 July 15.It was later determined that the optical maximum occurred on 2020 July 11 at 3.7 mag, making it visible to the naked eye. However, pre-discovery images from ASAS-SN indicate the eruption began on 2020 July 08 [79]. The optical spectrum evolved over the following days. Initially, YZ Ret was classified as a Fe II-type nova following the eruption onset and as a He/N-types on later days [80]. The WD in the system was estimated to be of the ONe type, based on an observed overabundance of oxygen [81].

An X-ray flash was detected a few hours before the optical rise on 2020 July 7 by the Spectrum–Roentgen–Gamma (SRG) instrument onboard of eROSITA. This event, lasting no more than eight hours, was recognized as the fireball phase. The spectrum during this phase was consistent with a blackbody at a temperature of 3×10^5 K [56]. The very short duration of the flash and the VY Scl classification of the system [79] constraint the mass of the WD, estimated to be $\leq 1.3 M_\odot$ [55].

Object	YZ Ret
Right ascension (RA, J2000)	$3^h 58^m 29.56^s$
Declination (Dec, J2000)	$-54°46'41.2''$
Galactic longitude (*l*, J2000)	$265°.3975$
Galactic latitude (*b*, J2000)	$-46°.3954$
Eruption date (t_0,UT)	2020-07-08.171

Table 4.1: Parameter of Nova YZ Ret

During the first two weeks the nova was detected in hard γ-rays (0.1-1 GeV) with Fermi-LAT, and in hard X-rays (3-79 keV) with NuSTAR. Spectral fitting revealed unusual abundances, suggesting a plasma either deficient in iron or overabundant in oxygen and neon [79]. NICER observations, starting on 2020 September 28, detected a super soft source (SSS) flux that was likely due to the ejecta being either shocked or photoionized, rather than emission from the WD. The low X-ray luminosity of only about $2.5 \times 10^{35} \, erg \, s^{-1}$ is attributed to the high inclination of the system, as no stellar continuum was detected [82].

The distance was estimated to be $d = 2.53^{+0.52}_{-0.26} Kpc$ by the Gaia/eDR3 catalogue [71]. Given its galactic coordinates (see Tab.4.1) the nova is located 1.8 kpc below the galactic disk. Due to its distance from the galactic plane the column density was estimated to be only $N_H = 1.2 \times 10^{20} \, cm^{-2}$ [82]. The orbital period was obtained by Schaefer et al. to be $P_{orb} = 3.18 \, hrs$ [83].

4.2 Diagnostic methods for high resolution spectra

High-resolution spectra enable us to determine the temperature, densities, and Emission Measure (EM) of the X-ray source. For YZ Ret, three diagnostic methods have been employed to accurately model the spectrum: He-like lines, the EM, and Radiative Recombination Continuum (RRC).

These methods are based on a collisional-radiative (CR) model, which assumes that all the ions are collisionally-ionized, excited by electrons and in a steady state. The predicted line intensity (in units of $ph \, s^{-1} cm^{-3}$) of a transition between two bound states *j* and *i*, where $j > i$ is:

$$I_{ji} = n_j A_{ji} \tag{4.1}$$

where n_j (cm^{-3}) is the number density of ions at level j and A_{ji} is the Einstein coefficient for spontaneous radiative decay. Electron temperatures T_e and densities n_e can be derive from the level population.

4.2.1   The Helium-like triplet diagnostic

A common diagnostic for X-ray sources involves the He-like triplet, which includes three key transitions from the $n = 2$ to the ground state $1s^2\,^1S_0$. These transitions are:

- From $1s2s\,^3S_1$ (forbidden line, denoted as *f*)

- From $1s2p\,^3P_{1,2}$ (intercombination lines, denoted as *i*)

- From $1s2p\,^1P_1$ (resonance line, denoted as *r*)

These lines are often referred to as w (resonance), *x* and y (intercombination) and *z* (forbidden), as shown in Fig.4.1 . Since the $1s2s$ is a metastable long-lived state, the line ratio can be expressed as follows:

$$R(n_e) = \frac{f}{i} \tag{4.2}$$

At low electron density the $n = 2$ levels decay radiatively, either directly to the ground state or via cascades. In this regime, the relative intensities of the forbidden, intercombination, and resonance lines are independent of electron density. However, as the n_e increases, collisional processes become significant and Eq.4.2 becomes sensitive to n_e when collisional de-excitations are comparable to spontaneous emissions. In this high-density regime, collisional excitations depopulate the $1s2s\,^3S_1$ level by exciting electrons to the $1s2p\,^3P_{1,2}$. This process reduces the intensity of the forbidden line and increases the intensity of the intercombination lines, leading to a decrease of the the ratio $R(n_e)$ [84].The electron density can be determined by computing the expected ratios from the CR model and comparing them with the observed ratios.

Figure 4.1: Simplified level scheme for Helium-like ions. w (or r), x,y (or i), and z (or f): resonance, intercombination, and forbidden lines, respectively. Full upward arrows: collisional excitation transitions, broken arrows: radiative transitions (including photo-excitation from $^3S_1$ to $^3P_{0,1,2}$ levels, and 2-photon continuum from $^1S_0$ to the ground level), and thick skew arrows: recombination plus cascade processes. From [84].

4.2.2   EM diagnostic

The emission measured can be used to derive the volume of the emitted plasma. Indeed the EM is define as $EM \sim n_e n_H V$, where n_H is the hydrogen column density. Once the distance d to the source is known, EM can be directly obtained both from the flux of the spectrum model F and the flux of discrete features like Radiative Recombination Continua, F^{RRC} (see Sec.4.2.3). In the first case, the flux in Xspec is parametrized as:

$$F = \frac{10^{-14} EM}{4\pi d^2} \tag{4.3}$$

Using the RRC, the formula becomes:

$$F^{RRC} = \frac{f_q A_Z \alpha^{RR} EM}{4\pi d^2} \tag{4.4}$$

where f_q is the ion fraction, A_Z the elemental abundance and α^{RR} is the Radiative Recombination rate coefficient.

4.2.3   The Radiative Recombination Continua (RRCs)

The high-resolution spectra from XMM and Chandra allow for the determination of electron temperature T_e and density using new diagnostics based on Radiative Recombination Continua. Radiative recombination occurs when an electron collides and recombines with an ion, emitting a photon in the process. This creates a continuous spectrum with sharp edges at the ionization energy of the atom E_{ion}, since the kinetic energy of the electron is not quantized. The energy distribution follows the Maxwell-Boltzmann one:

$$f(E) = \begin{cases} 0, & E < E_{ion} \\ \dfrac{C}{kT_e} e^{-\frac{(E-E_{ion})}{kT_e}} & E \geq E_{ion} \end{cases} \tag{4.5}$$

where C is the flux normalization constant. This feature of the spectrum is usually hard to discriminate from the continua, but in cold plasmas ($T_e \leq 10^5 \ K$) the RRC can be easily recognized providing a T_e diagnostic.

In the case of very bright RRC, also the Rydberg series of high-n converging onto it can be resolved, providing a density diagnostic. Collisional ionization rates increase with n, so at some n_{max} the observed X-ray line is dominated by collisional ionization rather than radiative decay,

truncating the series. Since collisional ionization rates S^{CI} increases with n_e while radiative decays do not, the upper and lower limits of n_e can be defined as:

$$\frac{A_{n_{max}+1},1}{S^{CI}_{n_{max}+1}} < n_e < \frac{A_{n_{max},1}}{S^{CI}_{n_{max}}} \tag{4.6}$$

So n_{max}, which is the effective width of the RRC edge, is a sensitive diagnostic of n_e.

4.3 Spectral analysis

4.3.1 The XMM Newton RGS spectrum

The nova was observed with the XMM Newton 77 days after the initial eruption. Observations took place from 2020 September 23 13:36 to 2020 September 23 21:22 UT (OBS ID: 0871010101; PI: Sokolovsky). Both RGS1 and RGS2 first order spectra were used covering the wavelength energy range $5 - 37\,\text{Å}$, namely $0.33 - 2.5\,\text{keV}$.

As shown in Fig.4.2 the RGS1 and RGS2 spectra display numerous features and various component were used to fit the spectra. The best-fit model includes:

- a `tbabs` component in order to model the galactic absorption, set to the value of $N_H = 1.2 \times 10^{20}\,cm^{-2}$.

- a `bvapec` representing the outflowing collisionally ionized plasma.

- three `redge` components to fit the RRCs of NV, CVI and CVI peaking respectively at $22.3\,,\,25.2$ and $31.45\,\text{Å}$.

- a series of `agauss` components to correct the amplitudes of the high-n lines converging to the CV and CVI RRCs.

Tab.4.2 and Fig.4.3 show the best fit parameters and the fitted spectrum respectively. The presence of the RRCs with $kT \sim 2\,\text{eV}$ indicates the existence of a colder plasma component interacting with the collisionally ionized plasma at $\sim 73\,\text{eV}$. From the redshift parameter of the `bvapec` component, we infer an outflow velocity of $\sim -1504\,km\,s^{-1}$, with the negative sign indicating a blueshift of the lines, meaning that the ejecta is outflowing toward us. The C abundance is set to the unity, since this is complemented by the RRC. Unfortunately the model

provides only the N and Ca abundances and an upper limit to the O abundance. Mg, Si, S, Ar and Fe were settled to the values obtained from the analysis of the Chandra spectrum and the remaining elements were assumed to be at solar values. As shown in *panel e* of Fig.4.3 satellite lines due to dielectronic recombination (DR Sat) are also present between 33.8-34.4 Å and 35-35.8 Å. This process occurs when an electron recombines with an ion in an excited state and excites a second electron simultaneously. The ion is left in a highly excited state, which may decay radiatively, creating a satellite line. These lines are named so because they appear at slightly longer wavelengths than the normal transitions from electrons in that energy level, due to the additional recombined electron being in an excited state.

XMM Newton	
Parameter	RGS
T_{bvapec}(eV)	73 ± 1
velocity$_{bvapec}$(km s^{-1})	-1504 ± 12
$\sigma_{v,\,bvapec}$(km s^{-1})	520 ± 4
$T_{CV\,RRC}$(eV)	1.96 ± 0.04
$T_{CVI\,RRC}$(eV)	1.9 ± 0.2
$T_{NVI\,RRC}$(eV)	≤ 1.5
C	1.00
N	0.81 ± 0.03
O	$\leq 5 \times 10^{-4}$
Ca	1.2 ± 0.1
$\text{Flux}^{a}_{bvapec} \times 10^{-3}\,ph\,cm^{-2}\,s^{-1}$	184 ± 2
$\text{Flux}^{b}_{CVRRC} \times 10^{-3}\,ph\,cm^{-2}\,s^{-1}$	24.2 ± 0.4
$\text{Flux}^{c}_{CVIRRC} \times 10^{-3}\,ph\,cm^{-2}\,s^{-1}$	0.5 ± 0.05
$\text{Flux}^{d}_{NVIRRC} \times 10^{-3}\,ph\,cm^{-2}\,s^{-1}$	0.05 ± 0.02

Table 4.2: Best fit parameters of the XMM Newton RGS model. **Notes.** [a] X-Ray flux of the bvapec component in the 0.3-0.7 keV range. [b] X-Ray flux of the CV RRC component in the 0.3-0.7 keV range. [c] X-Ray flux of the CVI RRC component in the 0.3-0.7 keV range. [d] X-Ray flux of the NVI RRC component in the 0.3-0.7 keV range.
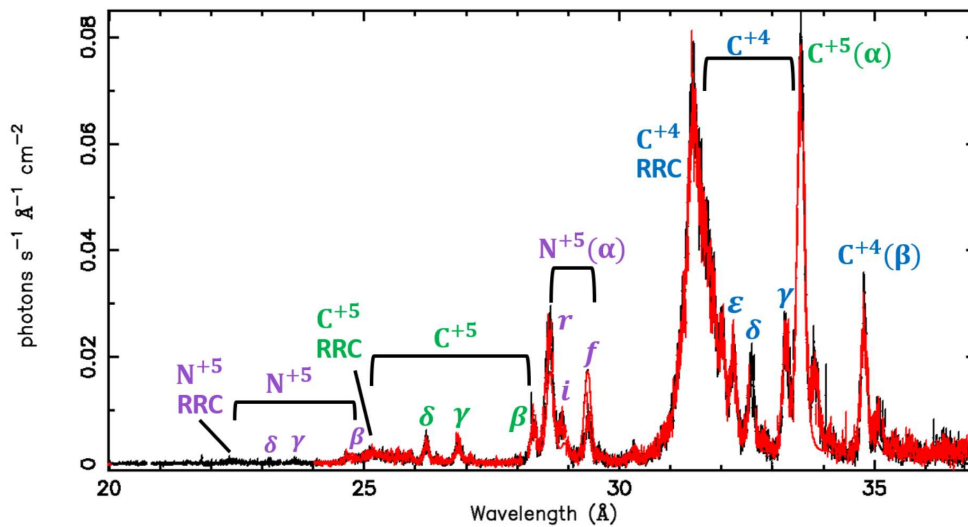
Figure 4.2: Fluxed spectrum of nova YZ Ret, observed in 2020-09-23 by XMM-Newton/RGS 77 days after the eruption. Black and red data are, respectively, RGS 1 and 2. Spectral lines of N^{+5}, C^{+4}, and C^{+5} are identified. The most prominent spectral feature is the narrow RRC of C^{+4} at 31.5Å, along with the C^{+4} He series converging to it. The much fainter narrow C^{+5} RRC is just barely observed around 25.2Å, along with the C^{+5} Lyman series. From [85]

Notes The notation used for the ions follows atomic physics conventions: C^{+4} corresponds to CV, C^{+5} to CVI, and N^{+5} to NVI. Greek letters denote the lines of the Lyman and He series converging to the RRCs.
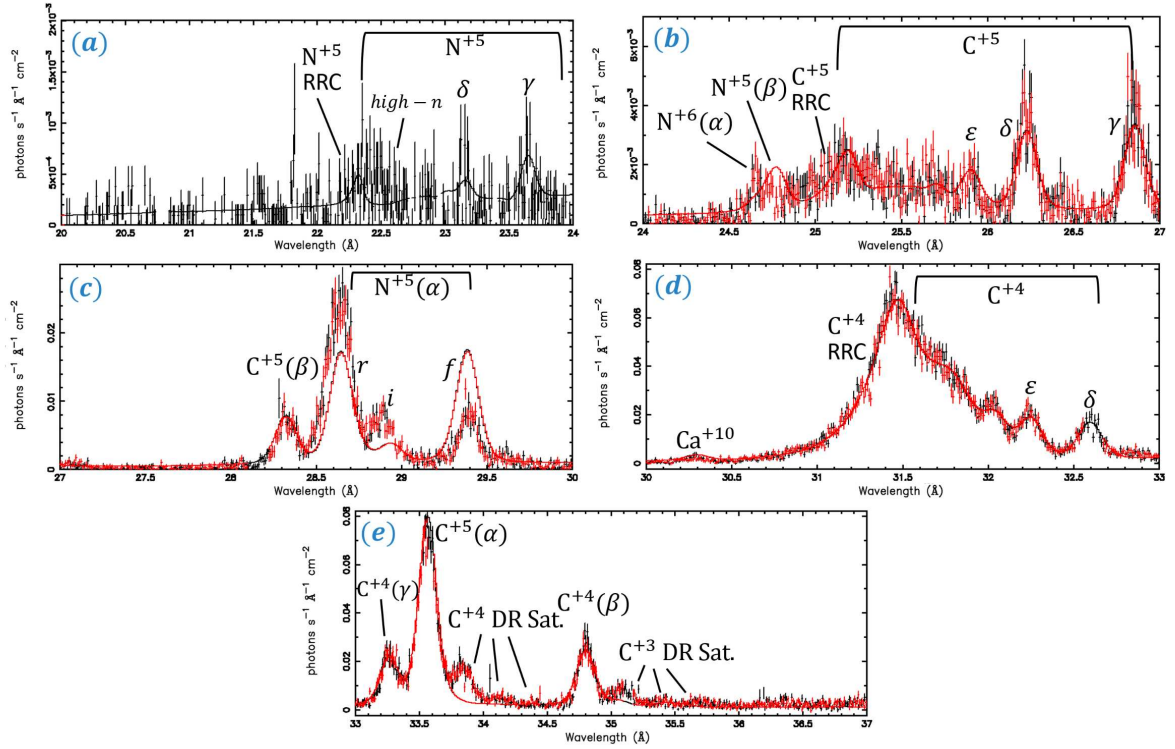
Figure 4.3: The full spectrum of YZ Ret observed by XMM-Newton RGS in the range of $20 - 37\text{Å}$. The spectrum shows emission lines of several ions such as C^{+4}, C^{+5}, N^{+5}. The solid line represents the fitted model of a velocity broadened collisionally ionized plasma (bvapec) with 3 colder RRC components for C^{+4}, C^{+5} and N^{+5} (redge), along with a series of gaussians to correct the amplitudes of the C^{+4} and C^{+5} high-n transitions (agauss). Note that the y-axis scale of the different panels is not the same. From [85].

Notes The notation used for the ions follows atomic physics conventions: C^{+4} corresponds to CV, C^{+5} to CVI, and N^{+5} to NVI. Greek letters denote the lines of the Lyman and He series converging to the RRCs.

4.3.2 The Chandra LETG spectrum

Observations with the Chandra LETG were conducted on 31 October 2020, 38 days after the XMM Newton observations and 115 days after the initial eruption. Due to the unavailability of the usual HRC-S+LETG combination, the HRC-I was used to obtain a spectrum in the $1.2 - 71\,\text{Å}$ range. The data were extracted using the Chandra CIAO data analysis package v 4.14.1., and the two first-order spectra were summed to increase the signal-to-noise ratio.

The spectrum analysis was performed with a binning of 20 counts per bin over the range of $10 - 70\,\text{Å}$. As the source was significantly fainter at this epoch compared to the XMM-Newton observations, the only prominent features were the CV RRC and thermal line emission of collisionally ionized plasma. The best fit model is a combination of $Tbabs \times (redge + bvapec)$. Tab.4.3 shows the best fit parameters, while Fig.4.4 illustrates the data along with the fitted model. The outflowing velocity, the CV RRC and collisionally ionized temperature are consistent with XMM Newton model. The cut-off energy of the `redge` component is set to 393.6 eV, corresponding to $31.5\,\text{Å}$, which is the peak wavelength of the CVI RRC. The kinematic broadening could not be constrained by the model and was fixed at the RGS best-fit value of $\sigma_v = 520\,kms^{-1}$. The N_H value of the `tbabs` component is set to $1.2 \times 10^{20}\,cm^{-2}$. The χ^2/d.o.f. is relatively low, as expected for high-resolution spectra. The LETG spectrum allows us to constraint the abundances of Mg, Si, S, Ar and Fe. Additionally, I classified the spectral lines across the entire spectrum using the ATOMDB tool [1]. The results are shown in Fig.4.5 and Tab.4.4.

---

[1]For more informations visit http://app.atomdb.org/
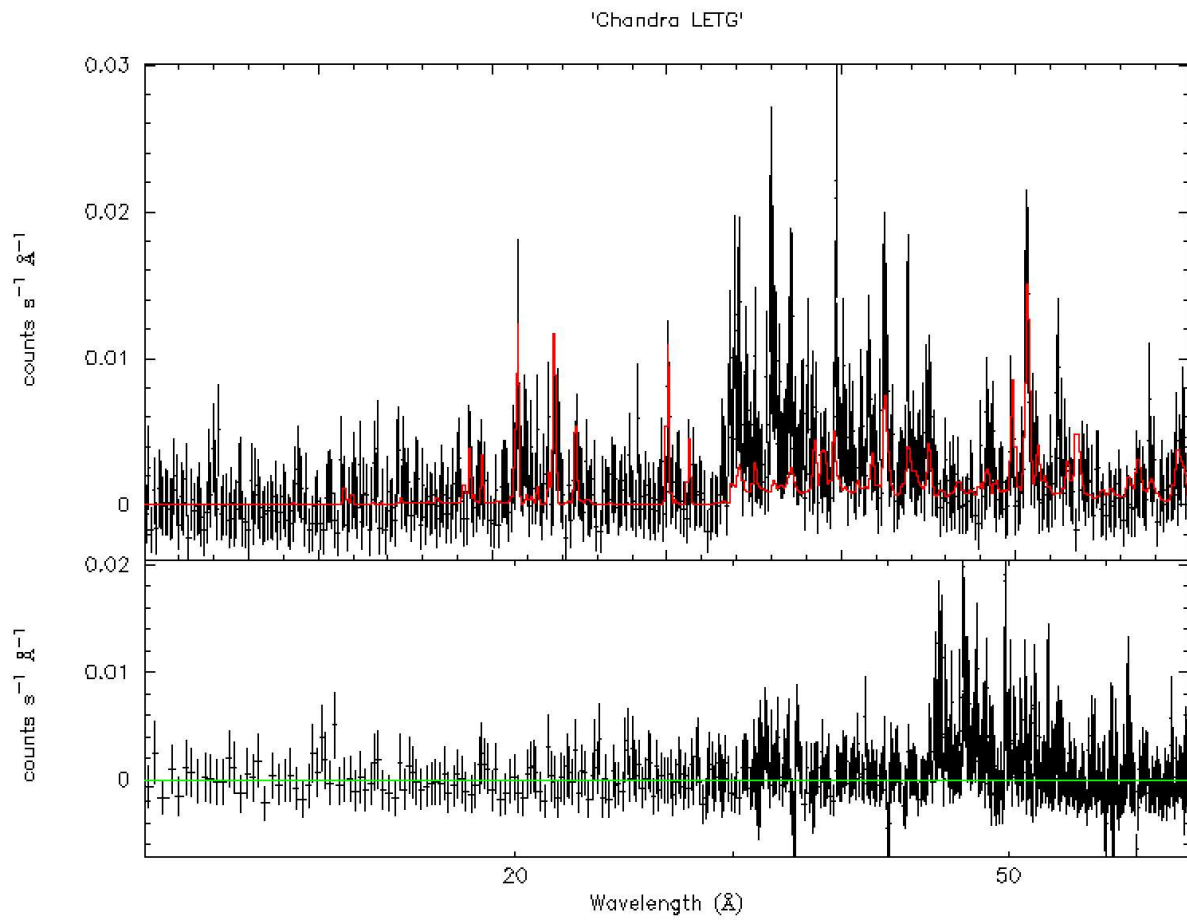
Figure 4.4: The spectrum of YZ Ret in the range $10 - 70\,\text{Å}$. The red solid line represent the fitting with the $Tbabs \times (redge + bvapec)$ model. The lower panel displays the residuals from the fit.

Chandra	
Parameter	LETG
$T_{\text{bvapec}}(eV)$	65 ± 5
$\text{velocity}_{\text{bvapec}}(\text{km } s^{-1})$	-1468 ± 90
$\text{norm}_{\text{bvapec}} \times 10^{-4}$	$7.05^{+3.80}_{-3.23}$
$T_{\text{CV RRC}}(eV)$	≤ 2.1
$\text{norm}_{\text{CV RRC}} \times 10^{-4}$	$467.8^{+105.7}_{-104.7}$
C	1.00
N	0.7 ± 0.4
O	≤ 0.2
Mg	1.5 ± 0.6
Ar	1.5 ± 0.4
Si	1.1 ± 0.4
S	1.7 ± 0.4
Ca	≤ 6.6
Fe	4.4 ± 3.3
$\text{Flux}^{a}_{bvapec} \times 10^{-3} \: ph \: cm^{-2} \: s^{-1}$	4.4 ± 0.5
$\text{Flux}^{b}_{CV RRC} \times 10^{-3} \: ph \: cm^{-2} \: s^{-1}$	0.9 ± 0.3
$\chi^{2}/\text{d.o.f.}$	0.75

Table 4.3: Best fit parameters of the $Tbabs \times (redge + bvapec)$ model. **Notes.** [a] X-Ray flux of the bvapec component in the 0.3-0.7 keV range. [b] X-Ray flux of the CV RRC component in the 0.3-0.7 keV range.

RGS	
Line	Wavelength (Å)
C V	31.481
C V	33.193
C VI	33.575
C IV	34.869
C V	40.069
Si IX	43.969
S X	44.500
Si IX	45.087
Fe XX	45.631
S XIII	45.969
Fe XVIII	46.106
S IX	47.206
Si X	48.088
Fe XIX	49.731
Si IX	52.481
Si IX	53.788
Fe XIII	60.606
Fe XII	62.513
Ni XII	67.656

Table 4.4: Identification of spectral lines in the Chandra LETG spectrum.
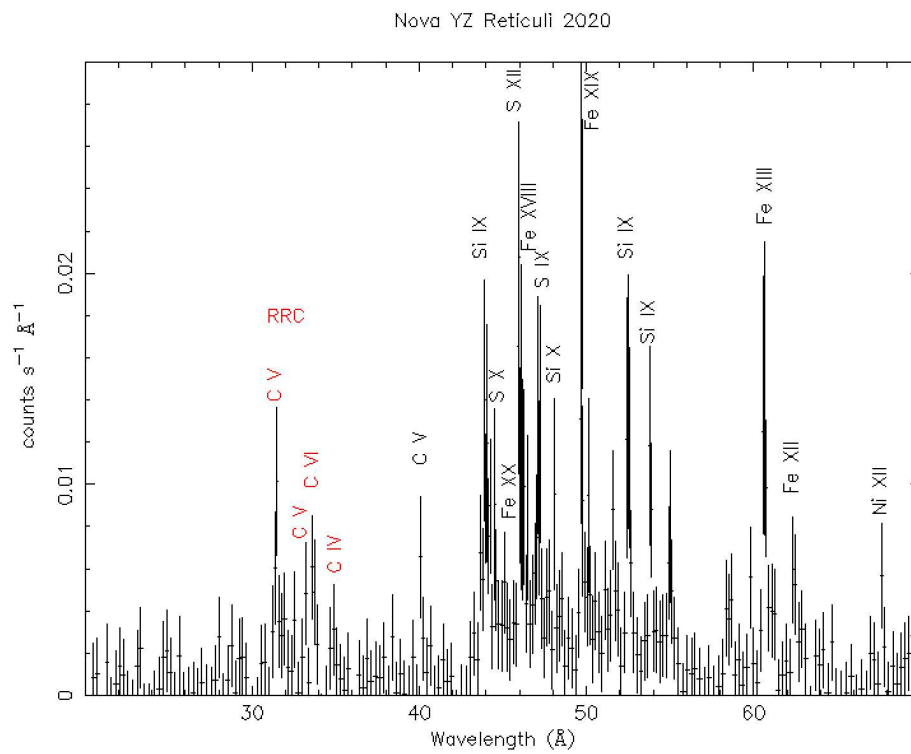
Figure 4.5: Spectral line classification of the Chandra LETG spectrum in the range of $20 - 70$ Å. The portion between $10 - 20$ Å is not shown as no lines were identified in that range. The RRC is highlighted in red.

4.4 Completion of the project with the atomic physics diagnostics

My collaborators, Dr. Ehud Behar and Sharon Mitrani, employed three different diagnostic methods as discussed in Sec.4.2 to derive the density and EM from the XMM Newton spectrum. Initially, the CV RRC was utilized to derive a density diagnostic. This region was modeled with RRC and a series of Gaussians representing the Rydberg series. The theoretical wavelengths of the unresolved CV lines from n to 1s transitions were calculated up to $n = 7$ using the Rydberg formula, with their Gaussian widths set to the best-fit value of $\sigma_v = 520 \, km \, s^{-1}$. The high-n levels were blended together, and their amplitudes up to $n = 9$ were fitted freely with Xspec. For $n \geq 10$ line intensities were scaled as n^{-3} to follow the Einstein coefficient trend. Once the wavelengths and widths of the lines were fixed, fits were performed by adding one Gaussian at a time to obtain a C_{stat} value [86]. The best fit was achieved when $n_{max} = 35$, corresponding to the minimum value of the C_{stat} function. A zoom into the CV RRC region between $30 - 33.5$Å is presented in Fig.4.6, along with the transitions up to 35. As shown in Fig.4.7, $\Delta C_{stat} = 1$, highlighted with black dots, corresponds to $n_{max} = 35^{+10}_{-5}$. To measure n_e from n_{max}, both A and S^{CI} are needed, which scale as n^{-3} and $n^2 log(n)$ [87], respectively, for $n \geq 10$. From Eq.4.6:

$$n_e \simeq \frac{A_{n_{max} \to 1}}{S^{CI}_{n_{max} \to \infty}} \propto \frac{n_{max}^{-5}}{log(n_{max})} \tag{4.7}$$

Using $n_{max} = 35^{+10}_{-5}$ the value of n_e can be found, which corresponds to $n_{e,CV} = (2.4^{+3.0}_{-1.8}) \times 10^{11} cm^{-3}$. Similarly, applying the same diagnostic to the CVI RRC observed at 25.2Å yields $n_{e,CVI} = (1.7 \pm 0.4) \times 10^{11} cm^{-3}$. Unfortunately, the low flux of the NVI RRC precludes the fitting of the high-n series and thus, no density diagnostic.

The plasma density was determined from the ratio of the NVI triplet lines, calculated using Eq.4.2. The intercombinatio(i), forbidden(f) and resonance(r) lines, fitted with the three gaussians, are presented in Fig.4.8. The measured $\frac{f}{i}$ ratio is $R(n_e)_{NVI} = 1.1 \pm 0.2$, indicating $n_{e,2eV} = (1.7 \pm 0.4) \times 10^{11} cm^{-3}$ for the cold $2 \, eV$ plasma component and $n_{e,70eV} = (5.8 \pm 0.7) \times 10^{10} cm^{-3}$ for the hot 70 eV plasma component. Fig.4.9 presents the computed $\frac{f}{i}$ ratio as a function of n_e. The density calculated for the $2 \, eV$ plasma component is consistent with the value obtained from the RRC measurement, while the density calculated for the $70 \, eV$ component is too low and falls
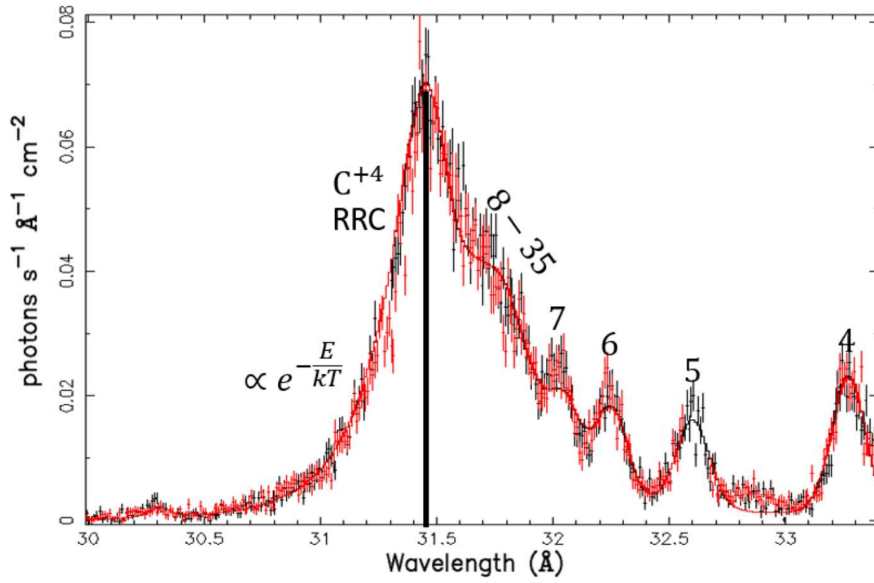
Figure 4.6: The 2020 RGS spectrum of YZ Ret in the range $30 - 33.5$Å highlighting the C^{+4} RRC region. Black and red data are RGS 1, and 2, respectively. The solid line is a model fitting the RRC, and the n to 1 Rydberg series up to n_{max} as gaussians. From [85].

Notes The notation used for the ions follows atomic physics conventions, so C^{+4} corresponds to CV.

outside the range inferred from the RRC.

The density n_e and the distance of YZ Ret were used to determined the emitted volume of both the hot and cold plasma components (see Sec.4.2.2). The calculations were performed using $d = (1.7 \pm 0.4) \times 10^{21} \, cm$ [71], a solar carbon abundance of $A_C = 4 \times 10^{-4}$ and the density value $n_{e,CVI} = (1.7 \pm 0.4) \times 10^{11} \, cm^{-3}$. For the cold plasma component Eq.4.4 was used together with the recombination coefficients $\alpha_{CV}^{RR} = 2.33 \times 10^{-12} \, cm^{-3} \, s^{-1}$ and $\alpha_{CVI}^{RR} = 3.15 \times 10^{-12} \, cm^{-3} \, s^{-1}$, to obtain $V_{CV} = (8 \pm 4) \times 10^{35} \, cm^{-3}$ and $V_{CVI} = (1.2 \pm 0.6) \times 10^{34} \, cm^3$ respectively. The volume of the hot plasma component is calculated from Eq.4.3, assuming $\dfrac{n_e}{n_H} = 1.2$ density ratio for a fully ionized, solar abundance plasma. The value obtained is $V_{hot} = (6 \pm 3) \times 10^{35} \, cm^{-3}$, which is consistent with the volume inferred for the cold component. This result confirms the mixing the two plasmas.
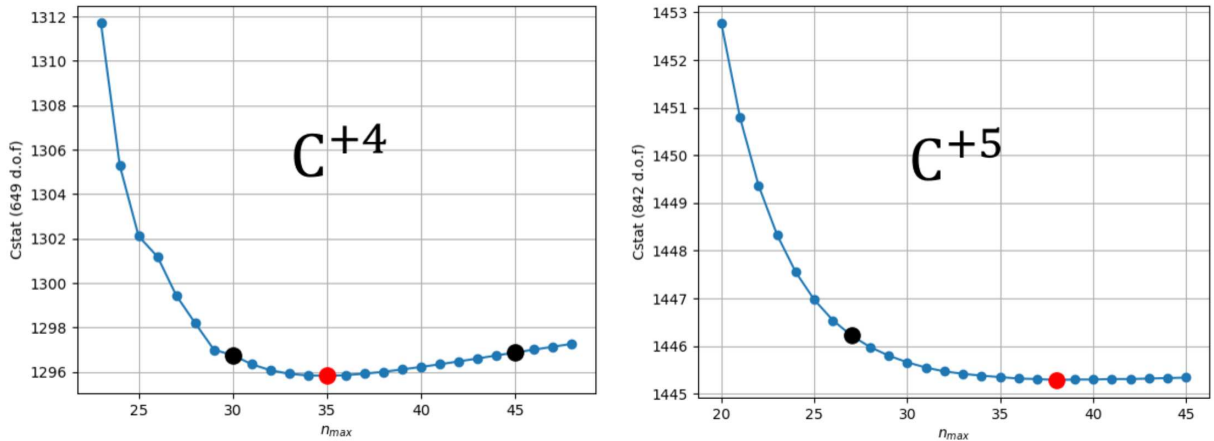
Figure 4.7: Values of C_{stat} obtained from fitting the Rydberg series up to n_{max}, the maximal $n \to 1$ transition included in the model for C^{+4} (left) and C^{+5} (right). The minimal C_{stat} value (red dot) and uncertainty region of $\Delta C_{stat} = 1$ (black dots) yield $n_{m}ax = 35^{+10}_{-5}$ for C^{+4}, and $n_{max} = 38(>27)$ for C^{+5}, which from Eq.4.6 indicates an electron density of $n_{e,RRC} = (2.4^{+3.0}_{-10}) \times 10^{11} cm^{-3}$ (for C^{+4}) and $n_{e,RRC} = (1.6(< 9.6)) \times 10^{11} cm^{-3}$ (for C^{+5}) at 90% confidence. From [85].

Notes The notation used for the ions follows atomic physics conventions: C^{+4} corresponds to CV and C^{+5} to CVI.
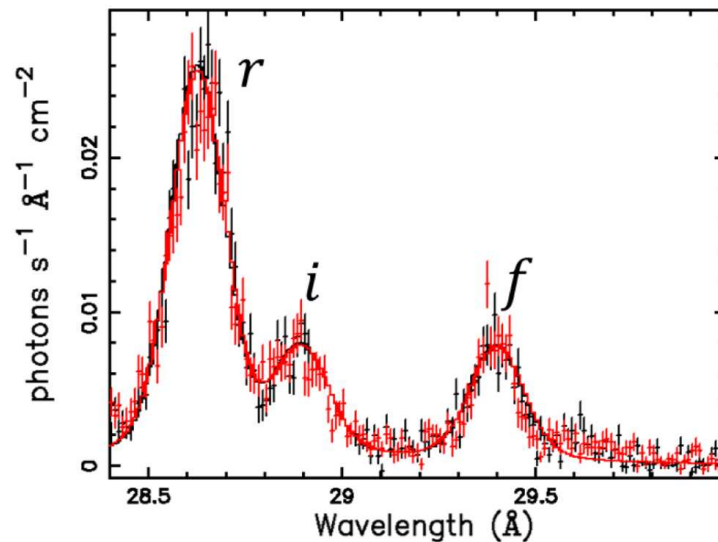
Figure 4.8: The r, i, f lines of NVI observed in the YZ Ret RGS spectrum. The measured $\frac{f}{i}$ ratio is 1.1 ± 0.2. From [85].
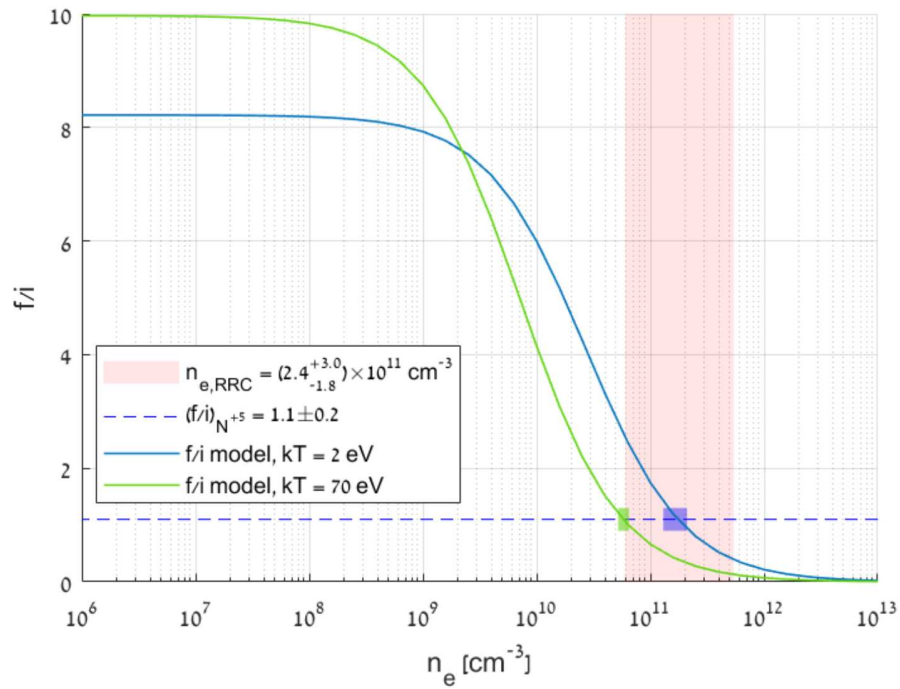
Figure 4.9: Computed $\frac{f}{i}$ ratio as a function of n_e for $kT_e = 2eV$ (blue) and 70eV (green). The blue dashed line is the measured $\frac{f}{i}$ ratio in the spectrum. Shaded areas indicate uncertainties. The measured ratio indicates a density of $n_e = (1.7 \pm 0.4) \times 10^{11} cm^{-3}$, for 2 eV, fully consistent with $n_{e,RRC} = \left(2.4^{+3.0}_{-1.8}\right) \times 10^{11} cm^{-3}$, which is represented by the red shaded area. From [85].

4.5   Discussion

Both X-ray spectra, obtained 77 and 115 days post-eruption, exhibit emission lines without any indication of thermal emission from the supersoft source (SSS).

Recombination and cooling timescales can be deduced from the electron density, $n_e = 10^{11}\,cm^{-3}$. For the CVI RRC $t_{rec} = \frac{1}{\alpha^{RR} n_e} \sim 30\,s$, using $\alpha = 3 \times 10^{-13}$. Instead the radiative cooling time for an ionized plasma at $kT = 70\,\text{eV}$ can be calculated from $\tau = \dfrac{kT}{n_e \Lambda} \simeq 10s$, with the cooling function $\Lambda \simeq 10^{-22} erg\,cm^3\,s^{-1}$. A longer recombination timescale compared to the cooling timescale suggests that these regions can remain ionized and emit energy for extended periods, implying continuous heating potentially attributed to a shock over the 38-day period.

The RGS and LEGT spectra exhibit both a hot and a cold plasma component, but the flux of the hot plasma dim by a factor 40 in the LEGT spectrum (see Tab.4.3 and Tab.4.2). However the outflow velocity remains constant at $\sim 1500\,km\,s^{-1}$, indicating that the shock front is moving outwards, reaching $\sim 2.5 \times 10^{14}\,cm$ during the RGS observations. The opening angle Ω of the flow can be determined using the thin shell geometry. According to this theory $V = \Omega r^2 \delta r$, where $\delta r \sim v\tau \sim 10^9\,cm$ is the width of the shell during the RGS epoch. Replacing $V_{hot} = (6\pm3) \times 10^{35}\,cm^{-3}$ and $r \sim 2.5 \times 10^{14}\,cm$ implies $\Omega \sim 8 \times 10^{-4}\,sr$, suggesting small blobs of the ejecta due to the narrow opening angle.

The connection between the hot and cold plasma can be deduced from their similar volumes and outflow velocities. In the case of YZ Ret, the charged ions may either be immersed within a dense cold gas or originate from impact with the accretion disk, contributing to the formation of the narrow RRC.

Chapter 5

Conclusions

Analyzing the XMM-Newton and Chandra X-ray spectra of novae during both quiescence and outburst phases provides valuable insights into the physics of these objects. In this thesis, I investigated two peculiar novae: V407 Lup, a member of the magnetic CV class, and YZ Ret, the first VY Scl type nova observed during an outburst.

Spectral and timing analysis of Nova V407 Lup during its quiescent phase confirmed its classification as an Intermediate Polar. The XMM-Newton EPIC spectra were modeled with either two thermal collisionally ionized plasma components at $\sim 0.17\,\mathrm{keV}$ and $\sim 24\,\mathrm{keV}$ or with a powerlaw with a flat slope $\alpha \sim 1$. The latter model suggested the possibility that V407 Lup hosts a pulsar white dwarf. Analysis of the XMM-Newton RGS spectrum revealed enhanced abundances of all elements relative to solar values, except for Mg, which showed strong depletion, and Fe and N, which mirrored solar abundances. Timing analysis confirmed the spin period of the WD $P_\omega \sim 564.64 \pm 0.64\,s$, corresponding to the period measured in outburst. Optical analysis pointed out the dispersion of the ejecta, as the [O III] were no longer detectable in 2022.

Observations of YZ Ret using two high-resolution gratings, XMM-Newton RGS and Chandra LETG, shortly after its outburst provided a unique opportunity to study a VY Scl nova in an unconventional phase. Both spectra were characterized by emission lines without signs of thermal emission from the supersoft source. The spectra revealed two plasma components: a hotter component at $\sim 70\,eV$ and a colder component at $\sim 2\,\mathrm{eV}$ inferred from the narrow RRC. The volumes of the two plasmas and the outflow velocity suggest a mixing between them. Density diagnostics, using both the NVI triplet and the RRCs, indicated an electron density $n_e \sim 10^{11}\,cm^{-3}$.

In summary, the detailed spectral and timing analysis of these two novae enhances our under-

standing of their physical properties and evolutionary states, contributing to our knowledge of cataclysmic variables.

Bibliography

[1] Robert Connon Smith (Jan. 2007). "Cataclysmic Variables". In: *arXiv e-prints*. DOI: 10.48550/arXiv.astro-ph/0701654.

[2] J.E. Pringle and R.A. Wade (1985). *Interacting binary stars*.

[3] Brian Warner (1998). "Cataclysmic Variable Stars". In: *Highlights of Astronomy* 11.1, 16–27. DOI: 10.1017/S1539299600019924.

[4] Brian Warner (1995). *Cataclysmic variable stars*. Vol. 28.

[5] Christian Knigge, Isabelle Baraffe, and Joseph Patterson (June 2011). "The Evolution of Cataclysmic Variables as Revealed by Their Donor Stars". In: *Astrophysical Journal, Supplement* 194.2, 28, p. 28. DOI: 10.1088/0067-0049/194/2/28. arXiv: 1102.2440.

[6] F. Verbunt and C. Zwaan (July 1981). "Magnetic braking in low-mass X-ray binaries." In: *Astronomy and Astrophysics* 100, pp. L7–L9.

[7] Matthias R. Schreiber, Diogo Belloni, and Axel D. Schwope (Feb. 2024). "The cataclysmic variable orbital period gap: More evident than ever". In: *Astronomy and Astrophysics* 682, L7, p. L7. DOI: 10.1051/0004-6361/202348807. arXiv: 2402.02076.

[8] Diogo Belloni et al. (Feb. 2020). "Evidence for reduced magnetic braking in polars from binary population models". In: *Monthly Notices of the RAS* 491.4, pp. 5717–5731. DOI: 10.1093/mnras/stz3413. arXiv: 1910.06333.

[9] J.E. Pringle (Jan. 1981). "Accretion discs in astrophysics". In: *Annual Review of Astron and Astrophysis* 19, pp. 137–162. DOI: 10.1146/annurev.aa.19.090181.001033.

[10] R.G.M. Rutten, J. van Paradijs, and J. Tinbergen (July 1992). "Reconstruction of the accretion disk in six cataclysmic variable stars." In: *Astronomy and Astrophysics* 260, pp. 213–226.

[11] J.C.B. Papaloizou and D.N.C. Lin (Jan. 1995). "Theory Of Accretion Disks I: Angular Momentum Transport Processes". In: *Annual Review of Astron and Astrophysis* 33, pp. 505–540. DOI: 10.1146/annurev.aa.33.090195.002445.

[12]   N.I. Shakura and R.A. Sunyaev (Jan. 1973). "Black holes in binary systems. Observational appearance." In: *Astronomy and Astrophysics* 24, pp. 337–355.

[13]   D. Lynden-Bell (Aug. 1969). "Galactic Nuclei as Collapsed Old Quasars". In: *Nature* 223.5207, pp. 690–694. DOI: 10.1038/223690a0.

[14]   G.T. Bath (Apr. 1985). "Cataclysmic novae". In: *Reports on Progress in Physics* 48.4, pp. 483–530. DOI: 10.1088/0034-4885/48/4/002.

[15]   S. Starrfield et al. (Sept. 2012). "Theoretical studies of accretion of matter onto white dwarfs and the single degenerate scenario for supernovae of Type Ia". In: *Bulletin of the Astronomical Society of India* 40, p. 419. DOI: 10.48550/arXiv.1210.6086. arXiv: 1210.6086.

[16]   Keegan J. Kelly et al. (Oct. 2013). "NUCLEAR MIXING METERS FOR CLASSICAL NOVAE". In: *The Astrophysical Journal* 777.2, p. 130. DOI: 10.1088/0004-637X/777/2/130. URL: https://dx.doi.org/10.1088/0004-637X/777/2/130.

[17]   O. Yaron et al. (Apr. 2005). "An Extended Grid of Nova Models. II. The Parameter Space of Nova Outbursts". In: *Astrophysical Journal* 623.1, pp. 398–410. DOI: 10.1086/428435. arXiv: astro-ph/0503143.

[18]   S. Starrfield et al. (Feb. 2009). "THE EFFECTS OF THE pep NUCLEAR REACTION AND OTHER IMPROVEMENTS IN THE NUCLEAR REACTION RATE LIBRARY ON SIMULATIONS OF THE CLASSICAL NOVA OUTBURST". In: *The Astrophysical Journal* 692.2, p. 1532. DOI: 10.1088/0004-637X/692/2/1532. URL: https://dx.doi.org/10.1088/0004-637X/692/2/1532.

[19]   William M. Wolf et al. (Oct. 2013). "HYDROGEN BURNING ON ACCRETING WHITE DWARFS: STABILITY, RECURRENT NOVAE, AND THE POST-NOVA SUPERSOFT PHASE". In: *The Astrophysical Journal* 777.2, p. 136. DOI: 10.1088/0004-637X/777/2/136. URL: https://dx.doi.org/10.1088/0004-637X/777/2/136.

[20]   Cecilia Helena Payne Gaposchkin (1957). *The galactic novae.* eng. Series in astrophysics. Amsterdam: North Holland.

[21]   Massimo della Valle and Mario Livio (Oct. 1995). "The Calibration of Novae as Distance Indicators". In: *Astrophysical Journal* 452, p. 704. DOI: 10.1086/176342.

[22] Bradley E. Schaefer (Dec. 2018). "The distances to Novae as seen by Gaia". In: *Monthly Notices of the RAS* 481.3, pp. 3033–3051. DOI: 10.1093/mnras/sty2388. arXiv: 1809.00180 [astro-ph.SR].

[23] Joanna Mikolajewska (Nov. 2010). "Symbiotic Novae". In: *arXiv e-prints*, arXiv:1011.5657, arXiv:1011.5657. DOI: 10.48550/arXiv.1011.5657. arXiv: 1011.5657.

[24] Lilia Ferrario, Domitilla de Martino, and Boris T. Gansicke (Oct. 2015). "Magnetic White Dwarfs". In: *Space Science Reviews* 191.1-4, pp. 111–169. DOI: 10.1007/s11214-015-0152-0. arXiv: 1504.08072.

[25] A.R. King and G. Shaviv (Dec. 984). "The hard X-ray light-curves of accreting magnetized white dwarfs." In: *Monthly Notices of the RAS* 211, pp. 883–893. DOI: 10.1093/mnras/211.4.883.

[26] T.L. Parker, A.J. Norton, and K. Mukai (Aug. 2005). "X-ray orbital modulations in intermediate polars". In: *Astronomy and Astrophysics* 439.1, pp. 213–225. DOI: 10.1051/0004-6361:20052887. arXiv: astro-ph/0503658.

[27] F. Bernardini et al. (June 2012). "Characterization of new hard X-ray cataclysmic variables". In: *Astronomy and Astrophysics* 542, A22, A22. DOI: 10.1051/0004-6361/201219233. arXiv: 1204.3758.

[28] Manabu Ishida and Hiroyuki Ezuk (Jan. 1999). "Iron Line Diagnostics of the Post-Shock Hot Plasma in Magnetic Cataclysmic Variables observed with ASCA". In: Astronomical Society of the Pacific Conference Series 157. Ed. by Coel Hellier and Koji Mukai, p. 333.

[29] Coel Hellier (Oct. 1997). "The size of the accretion region in intermediate polars: eclipses of XY ARIETIS observed with RXTE". In: *Monthly Notices of the RAS* 291.1, pp. 71–80. DOI: 10.1093/mnras/291.1.71. arXiv: astro-ph/9708076.

[30] Ryuichi Fujimoto and Manabu Ishida (Jan. 1997). "X-Ray Spectroscopic Observations of EX Hydrae and Mass Determination of the White Dwarf". In: *The Astrophysical Journal* 474.2, p. 774. DOI: 10.1086/303483. URL: https://dx.doi.org/10.1086/303483.

[31] D.Q. Lamb and A.R. Masters (Dec. 1979). "X and UV radiation from accreting magnetic degenerate dwarfs." In: *Astrophysical Journal* 234, pp. L117–L122. DOI: 10.1086/183121.

[32] J. Bailey (Jan. 1996). "Accretion phenomena in cataclysmic variables". In: *Publications of the Astron. Soc. of Australia* 13.1, pp. 75–80. DOI: 10.1017/S1323358000020579.

[33] G. Anzolin et al. (Oct. 2008). "Two new intermediate polars with a soft X-ray component". In: *Astronomy and Astrophysics* 489.3, pp. 1243–1254. DOI: 10.1051/0004-6361:200810402. arXiv: 0808.1499.

[34] V. Suleimanov, M. Revnivtsev, and H. Ritter (May 2005). "RXTE broadband X-ray spectra of intermediate polars and white dwarf mass estimates". In: *Astronomy and Astrophysics* 435.1, pp. 191–199. DOI: 10.1051/0004-6361:20041283. arXiv: astro-ph/0405236.

[35] K. Aizu (Apr. 1973). "X-Ray Emission Region of a White Dwarf with Accretion". In: *Progress of Theoretical Physics* 49.4, pp. 1184–1194. DOI: 10.1143/PTP.49.1184.

[36] J. Brunschweiger et al. (Mar. 2009). "Intermediate polars in the Swift/BAT survey: spectra and white dwarf masses". In: *Astronomy and Astrophysics* 496.1, pp. 121–127. DOI: 10.1051/0004-6361/200811285. arXiv: 0901.3562.

[37] Mario Livio, Anurag Shankar, and James W. Truran (July 1988). "Nova Outbursts on Magnetic White Dwarfs". In: *Astrophysical Journal* 330, p. 264. DOI: 10.1086/166470.

[38] M. Orio, E. Trussoni, and H. Oegelman (Apr. 1992). "Classical novae as fast magnetic rotators." In: *Astronomy and Astrophysics* 257, pp. 548–556.

[39] R. K. Honeycutt and S. Kafka (Sept. 2004). "Characteristics of High-State/Low-State Transitions in VY Sculptoris Stars". In: *The Astronomical Journal* 128.3, p. 1279. DOI: 10.1086/422737. URL: https://dx.doi.org/10.1086/422737.

[40] D. W. Hoard et al. (Apr. 2014). "NOVA-LIKE CATACLYSMIC VARIABLES IN THE INFRARED". In: *The Astrophysical Journal* 786.1, p. 68. DOI: 10.1088/0004-637X/786/1/68. URL: https://dx.doi.org/10.1088/0004-637X/786/1/68.

[41] V.S. Dhillon (Jan. 1996). "The Nova-like variables". In: Astrophysics and Space Science Library 208. Ed. by A. Evans and Janet H. Wood, p. 3. DOI: 10.1007/978-94-009-0325-8_1. arXiv: astro-ph/9509156.

[42] D. W. Hoard et al. (Oct. 2010). "SIMULTANEOUS X-RAY AND ULTRAVIOLET OBSERVATIONS OF THE SW SEXTANTIS STAR DW URSAE MAJORIS". In: *The Astronomical Journal* 140.5, p. 1313. DOI: 10.1088/0004-6256/140/5/1313. URL: https://dx.doi.org/10.1088/0004-6256/140/5/1313.

[43] P. Rodriguez-Gil et al. (Jan. 2002). "Detection of variable circular polarization in the SW Sex star V795 Herculis". In: Astronomical Society of the Pacific Conference Series 261. Ed. by

B.T. Gansicke, K. Beuermann, and K. Reinsch, p. 533. DOI: 10.48550/arXiv.astro-ph/0110173. arXiv: astro-ph/0110173.

[44] Pablo Rodríguez-Gil et al. (Feb. 2001). "Evidence of Magnetic Accretion in an SW Sextantis Star: Discovery of Variable Circular Polarization in LS Pegasi". In: *The Astrophysical Journal* 548.1, p. L49. DOI: [10.1086/318922](10.1086/318922). URL: https://dx.doi.org/10.1086/318922.

[45] L. Schmidtobreick (Jan. 2013). "The SW Sex Phenomenon as an Evolutionary Stage of Cataclysmic Variables". In: *Central European Astrophysical Bulletin* 37, pp. 361–368. DOI: 10.48550/arXiv.1211.2171. arXiv: [1211.2171](1211.2171).

[46] P. Zemko and T. Kato (Mar. 2014). "Photometric analysis of TT Arietis in the high and low states during 2004-2013". In: *Contributions of the Astronomical Observatory Skalnate Pleso* 43.3, pp. 487–489.

[47] K. Wu, D.T. Wickramasinghe, and B. Warner (Apr. 1995). "Feedback Mass Transfer in Cataclysmic Variables - an Explanation of the Behaviour of Vy-Sculptoris". In: *Publications of the ASP* 12.1, p. 60. DOI: [10.1017/S132335800002004X](10.1017/S132335800002004X).

[48] M. Livio and J.E. Pringle (June 1994). "Star Spots and the Period Gap in Cataclysmic Variables". In: *Astrophysical Journal* 427, p. 956. DOI: [10.1086/174202](10.1086/174202).

[49] R. Leach et al. (May 1999). "The light curves of VY Scl stars". In: *Monthly Notices of the RAS* 305.1, pp. 225–230. DOI: [10.1046/j.1365-8711.1999.02450.x](10.1046/j.1365-8711.1999.02450.x).

[50] R.E. Williams et al. (Aug. 1991). "The Evolution and Classification of Postoutburst Novae Spectra". In: *Astrophysical Journal* 376, p. 721. DOI: [10.1086/170319](10.1086/170319).

[51] F.A. Ringwald, T. Naylor, and K. Mukai (July 1996). "The optical spectra of old novae". In: *Monthly Notices of the RAS* 281.1, pp. 192–210. DOI: 10.1093/mnras/281.1.192.

[52] E. Aydi et al. (Jan. 2024). "Revisiting the classics: on the evolutionary origin of the 'Fe II' and 'He/N' spectral classes of novae". In: *Monthly Notices of the RAS* 527.3, pp. 9303–9321. DOI: 10.1093/mnras/stad3342. arXiv: [2309.07097](2309.07097).

[53] Robert E. Williams (Aug. 1992). "The Formation of Novae Spectra". In: *Astronomical Journal* 104, p. 725. DOI: [10.1086/116268](10.1086/116268).

[54] K.V. Sokolovsky et al. (June 2023). "The multiwavelength view of shocks in the fastest nova V1674 Her". In: *Monthly Notices of the RAS* 521.4, pp. 5453–5472. DOI: 10.1093/mnras/stad887. arXiv: [2302.03043](2302.03043).

[55] Mariko Kato, Hideyuki Saio, and Izumi Hachisu (Aug. 2022). "A Light-curve Analysis of the X-Ray Flash First Observed in Classical Novae". In: *Astrophysical Journal, Letters* 935.1, L15, p. L15. DOI: 10.3847/2041-8213/ac85c1. arXiv: 2208.01249.

[56] Ole Konig et al. (May 2022). "X-ray detection of a nova in the fireball phase". In: *Nature* 605.7909, pp. 248–250. DOI: 10.1038/s41586-022-04635-y. arXiv: 2209.05125.

[57] Laura Chomiuk, Brian D. Metzger, and Ken J. Shen (Sept. 2021). "New Insights into Classical Novae". In: *Annual Review of Astron and Astrophysis* 59, pp. 391–444. DOI: 10.1146/annurev-astro-112420-114502. arXiv: 2011.08751.

[58] M. Orio et al. (June 2020). "Chandra High Energy Transmission Gratings Spectra of V3890 Sgr". In: *Astrophysical Journal* 895.2, 80, p. 80. DOI: 10.3847/1538-4357/ab8c4d. arXiv: 2004.11263.

[59] A.C. Gordon et al. (Apr. 2021). "Surveying the X-Ray Behavior of Novae as They Emit γ-Rays". In: *Astrophysical Journal* 910.2, 134, p. 134. DOI: 10.3847/1538-4357/abe547. arXiv: 2010.15930.

[60] J. U. Ness et al. (Nov. 2013). "Obscuration effects in super-soft-source X-ray spectra". In: *Astronomy and Astrophysics* 559, A50, A50. DOI: 10.1051/0004-6361/201322415. arXiv: 1309.2604.

[61] M. Orio et al. (Aug. 2018). "What We Learn from the X-Ray Grating Spectra of Nova SMC 2016". In: *Astrophysical Journal* 862.2, 164, p. 164. DOI: 10.3847/1538-4357/aacf06. arXiv: 1806.08249.

[62] D. de Martino et al. (Sept. 2020). "Hard X-ray cataclysmic variables". In: *Advances in Space Research* 66.5, pp. 1209–1225. DOI: 10.1016/j.asr.2019.09.006. arXiv: 1909.06306.

[63] F. Jansen et al. (Jan. 2001). "XMM-Newton observatory. I. The spacecraft and operations". In: *Astronomy and Astrophysics* 365, pp. L1–L6. DOI: 10.1051/0004-6361:20000036.

[64] M.J.L. Turner et al. (Jan. 2001). "The European Photon Imaging Camera on XMM-Newton: The MOS cameras". In: *Astronomy and Astrophysics* 365, pp. L27–L35. DOI: 10.1051/0004-6361:20000087. arXiv: astro-ph/0011498 [astro-ph].

[65]   J.W. den Herder et al. (Jan. 2001). "The Reflection Grating Spectrometer on board XMM-Newton". In: *Astronomy and Astrophysics* 365, pp. L7–L17. DOI: 10 . 1051 / 0004 –6361:20000058.

[66]   J. Wilms, A. Allen, and R. McCray (Oct. 2000). "On the Absorption of X-Rays in the Interstellar Medium". In: *Astrophysical Journal* 542.2, pp. 914–924. DOI: 10.1086/317016. arXiv: astro-ph/0008425.

[67]   Randall K. Smith et al. (Aug. 2001). "Collisional Plasma Models with APEC/APED: Emission-Line Diagnostics of Hydrogen-like and Helium-like Ions". In: *Astrophysical Journal, Letters* 556.2, pp. L91–L95. DOI: 10.1086/322992. arXiv: astro-ph/0106478.

[68]   K.Z. Stanek et al. (Sept. 2016). "ASAS-SN Discovery of A Likely Galactic Nova ASASSN-16kt at V=9.1". In: *The Astronomer's Telegram* 9538, p. 1.

[69]   E. Aydi et al. (Oct. 2018). "Multiwavelength observations of V407 Lupi (ASASSN-16kt), a very fast nova erupting in an intermediate polar". In: *Monthly Notices of the RAS* 480.1, pp. 572–609. DOI: 10.1093/mnras/sty1759. arXiv: 1807.00706.

[70]   L. Izzo et al. (Aug. 2018). "Beryllium detection in the very fast nova ASASSN-16kt (V407 Lupi)". In: *Monthly Notices of the RAS* 478.2, pp. 1601–1610. DOI: 10 . 1093 / mnras /sty435. arXiv: 1802.05896.

[71]   C. A. L. Bailer-Jones et al. (Feb. 2021). "Estimating Distances from Parallaxes. V. Geometric and Photogeometric Distances to 1.47 Billion Stars in Gaia Early Data Release 3". In: *The Astronomical Journal* 161.3, p. 147. DOI: 10 . 3847 / 1538 – 3881 / abd806. URL: https://dx.doi.org/10.3847/1538-3881/abd806.

[72]   J.D. Scargle (Dec. 1982). "Studies in astronomical time series analysis. II. Statistical aspects of spectral analysis of unevenly spaced data." In: *Astrophysical Journal* 263, pp. 835–853. DOI: 10.1086/160554.

[73]   Astropy Collaboration et al. (Oct. 2013). "Astropy: A community Python package for astronomy". In: *Astronomy and Astrophysics* 558, A33, A33. DOI: 10.1051/0004-6361/201322068. arXiv: 1307.6212.

[74]   Astropy Collaboration et al. (Sept. 2018). "The Astropy Project: Building an Open-science Project and Status of the v2.0 Core Package". In: *Astronomical Journal* 156.3, 123, p. 123. DOI: 10.3847/1538-3881/aabc4f. arXiv: 1801.02634.

[75] Astropy Collaboration et al. (Aug. 2022). "The Astropy Project: Sustaining and Growing a Community-oriented Open-source Project and the Latest Major Release (v5.0) of the Core Package". In: *Astrophysical Journal* 935.2, 167, p. 167. DOI: 10.3847/1538-4357/ac7c74. arXiv: 2206.14220.

[76] Jonathan Schachter et al. (June 1991). "Bowen Fluorescence in AM Herculis Stars". In: *Astrophysical Journal* 373, p. 633. DOI: 10.1086/170083.

[77] T.R. Marsh et al. (Sept. 2016). "A radio-pulsing white dwarf binary star". In: *Nature* 537.7620, pp. 374–377. DOI: 10.1038/nature18620. arXiv: 1607.08265.

[78] Ingrid Pelisoli et al. (Jan. 2024). "Unveiling the white dwarf in J191213.72 - 441045.1 through ultraviolet observations". In: *Monthly Notices of the RAS* 527.2, pp. 3826–3836. DOI: 10.1093/mnras/stad3442. arXiv: 2311.05558.

[79] Kirill V. Sokolovsky et al. (Aug. 2022). "The first nova eruption in a novalike variable: YZ Ret as seen in X-rays and γ-rays". In: *Monthly Notices of the RAS* 514.2, pp. 2239–2258. DOI: 10.1093/mnras/stac1440. arXiv: 2108.03241.

[80] A. Carr et al. (July 2020). "WiFeS follow-up observations of the naked-eye nova associated to MGAB-V207". In: *The Astronomer's Telegram* 13874, p. 1.

[81] L. Izzo et al. (Sept. 2020). "UVES observations of Nova Reticuli 2020 during Minimal Science Operations show it is entering the nebular phase". In: *The Astronomer's Telegram* 14048, p. 1.

[82] M. Orio et al. (June 2022). "NICER Monitoring of Supersoft X-Ray Sources". In: *Astrophysical Journal* 932.1, 45, p. 45. DOI: 10.3847/1538-4357/ac63be. arXiv: 2204.01660.

[83] Bradley E. Schaefer (Dec. 2022). "Comprehensive listing of 156 reliable orbital periods for novae, including 49 new periods". In: *Monthly Notices of the RAS* 517.3, pp. 3640–3659. DOI: 10.1093/mnras/stac2089. arXiv: 2207.02932.

[84] Jacques Dubau and Delphine Porquet (Apr. 2002). "Helium-like triplet diagnostics". In: *arXiv e-prints*, astro-ph/0204049, astro–ph/0204049. DOI: 10.48550/arXiv.astro-ph/0204049. arXiv: astro-ph/0204049.

[85] Sharon Mitrani et al. (May 2024). "Mixing of hot shocked plasma with cold gas in Nova YZ Ret 2020". In: *arXiv e-prints*, arXiv:2405.09219, arXiv:2405.09219. DOI: 10.48550/arXiv.2405.09219. arXiv: 2405.09219.

[86] W. Cash (Mar. 1979). "Parameter estimation in astronomy through application of the likelihood ratio." In: *Astrophysical Journa* 228, pp. 939–947. DOI: 10.1086/156922.

[87] Wolfgang Lotz (June 1968). "Electron-impact ionization cross-sections and ionization rate coefficients for atoms and ions from hydrogen to calcium". In: *Zeitschrift fur Physik* 216.3, pp. 241–247. DOI: 10.1007/BF01392963.